

1 GEFSv12 reforecast dataset for supporting subseasonal and
2 hydrometeorological applications

3
4 Hong Guan¹, Yuejian Zhu², Eric Sinsky³, Bing Fu³, Wei Li³, Xiaqiong Zhou⁴, Xianwu Xue¹,
5 Dingchen Hou², Jiayi Peng³, M. M. Nageswararao⁵, Vijay Tallapragada², Thomas M.
6 Hamill⁶, Jeffrey S. Whitaker⁶, Gary Bates⁷, Philip Pegion⁶, Sherrie Frederick^{6,7}, Matthew
7 Rosencrans⁸, Arun Kumar⁸

8
9 ¹SRG at NOAA/NWS/NCEP/EMC, College Park, Maryland

10 ²NOAA/NWS/NCEP/EMC, College Park, Maryland

11 ³IMSG at NOAA/NWS/NCEP/EMC, College Park, Maryland

12 ⁴CPAESS, University Corporation for Atmospheric Research at NOAA/NWS/NCEP/EMC
13 and NOAA/OAR/GFDL, Princeton, New Jersey

14 ⁵CPAESS, University Corporation for Atmospheric Research at NOAA/NWS/NCEP/EMC,
15 College Park, Maryland

16 ⁶NOAA Physical Sciences Laboratory, Boulder, Colorado

17 ⁷Cooperative Institute for Research in Environmental Sciences, University of Colorado,
18 Boulder

19 ⁸NOAA/NWS/NCEP/CPC, College Park, Maryland

20
21 Submitted to *Monthly Weather Review*

22 17 December 2021

23
24 Corresponding author:

25
26 Dr. Hong Guan

27 5830 University Research Ct,

28 College Park, MD 20740

29 Email: Hong.Guan@noaa.gov

30 **Abstract**

31
32 For the newly implemented Global Ensemble Forecast System version 12 (GEFSv12),
33 a 31-year (1989-2019) ensemble reforecast dataset has been generated at the National Centers
34 for Environmental Prediction (NCEP). The reforecast system is based on NCEP's Global
35 Forecast System version 15.1 and GEFSv12, which uses the Finite Volume 3 dynamical core.
36 The resolution of the forecast system is ~25 km with 64 vertical hybrid levels. The Climate
37 Forecast System (CFS) reanalysis and GEFSv12 reanalysis serve as initial conditions for the
38 Phase 1 (1989–1999) and Phase 2 (2000–2019) reforecasts, respectively. The perturbations
39 were produced using breeding vectors and ensemble transforms with a rescaling technique for
40 Phase 1 and ensemble Kalman filter 6-h forecasts for Phase 2. The reforecasts were initialized
41 at 0000 (0300) UTC once per day out to 16 days with 5 ensemble members for Phase 1 (Phase
42 2), except on Wednesdays when the integrations were extended to 35 days with 11 members.
43 The reforecast data set was produced on NOAA's Weather and Climate Operational
44 Supercomputing System at NCEP.

45 This study summarizes the configuration and dataset of the GEFSv12 reforecast and
46 presents some preliminary evaluations of 500hPa geopotential height, tropical storm track,
47 precipitation, 2-meter temperature, and MJO forecasts. The results were also compared with
48 GEFSv10 or GEFS Subseasonal Experiment reforecasts. In addition to supporting calibration
49 and validation for the National Water Center, NCEP Climate Prediction Center, and other
50 National Weather Service stakeholders, this high-resolution subseasonal dataset also serves as
51 a useful tool for the broader research community in different applications.

53 **1. Introduction**

54 The important role of a reforecast in validating and calibrating weather and climate
55 model forecasts (Hamill et al. 2004, 2006, 2013, 2015; Hamill and Whitaker 2006; Wilks and
56 Hamill 2007; Hagedorn et al. 2008, 2012; Hagedorn 2008; Hamill 2012; Hamill and Kiladis
57 2013; Baxter et al. 2014; Scheuerer and Hamill 2015; Ou et al. 2016; Guan et al. 2015, 2019;
58 Gascon et al. 2019), diagnosing model errors (Hamill et al. 2013), and predicting extreme or
59 rare events (Hagedorn 2008; Hamill et al. 2008, 2013; Guan and Zhu 2017; Nardi et al. 2018;
60 and Li et al. 2019) has been widely recognized. Currently, reforecast datasets are utilized
61 operationally at several weather-climate centers worldwide. For instance, a reforecast dataset
62 is used to calibrate forecasts at the Canadian Meteorological Center (CMC), the National
63 Centers for Environmental Prediction (NCEP), and European Centre for Medium-Range
64 Weather Forecasts (ECMWF) to improve numerical weather guidance for a variety of forecast
65 timescales. In combination with an analysis climatology, a reforecast (i.e., model) climatology
66 is also employed to provide real-time extreme weather forecasts for some common concern
67 weather elements at NCEP (Guan and Zhu 2017) and ECMWF (LaLaurette 2003; Hagedorn
68 2008). Reforecasts are used extensively in conjunction with hydrologic prediction (DeMargne
69 et al. 2014; Scheuerer and Hamill 2018; Emerton et al. 2018). More recently, as part of the
70 Subseasonal Experiment (SubX; Pegion et al. 2019), seven modeling groups from the U.S. and
71 Canada generated reforecast datasets, separately. The combined datasets provide a foundation
72 for employing current best practice methods for real-time weeks 3 and 4 outlooks of hazardous
73 and extreme events at the NCEP Climate Prediction Center (CPC).

74 Ideally, creating a reforecast dataset requires a set of consistent reanalysis data as initial
75 conditions. Both reforecast and reanalysis should also employ the same model system that is
76 used in the actual real-time forecast, ideally at the same resolution. However, generating a full
77 dataset for a reanalysis and reforecast, usually from 10 years to several decades of data, is an
78 extremely time- and labor-intensive procedure and impractical in operational forecasting.
79 Therefore, an inconsistent initial analysis had been used for the GEFSv11 (Guan and Zhu 2017)
80 and GEFS-SubX reforecasts. For example, the 17 years (1999–2015) of GEFS_SubX
81 reforecasts (Zhu et al. 2018; Li et al. 2019; Guan et al. 2019) used the Climate Forecast System

82 Reanalysis (CFSR) and Global Data Assimilation System (GDAS) as the initial conditions for
83 1999–2010 and 2011–2016, respectively. In addition to the inconsistency of the analysis itself,
84 the forecast systems generating the reanalysis are also quite different from the reforecast and
85 real-time forecast systems. This inconsistency in reanalysis has resulted in a difference in the
86 2-m temperature bias characteristics (Hamill 2017; Guan et al. 2019), especially for short lead
87 times when initial conditions play a critical role in the forecast. This further confirms the strong
88 desirability of simultaneously generating reanalysis and reforecast data in the operational
89 implementation.

90 On September 23, 2020, the FV3 (Finite-Volume)-based Global Ensemble Forecast
91 System version 12 (GEFSv12) was implemented at the National Oceanic and Atmospheric
92 Administration (NOAA). To provide seamless numerical guidance to a broad range of users
93 and partners, the integration time of the GEFSv12 was extended from week 1 (weather
94 forecasts) and week 2 (extended forecasts) to weeks 3-5 (subseasonal forecasts).
95 Accompanying the GEFSv12 implementation, 20-year reanalysis and 31-year reforecast
96 datasets were also simultaneously produced by NOAA’s Physical Science Laboratory (PSL)
97 and Environmental Modelling Center (EMC), respectively, to support stakeholders CPC and
98 the National Water Center (NWC) for subseasonal and hydrological applications. This marks
99 the first official generation of a reanalysis/reforecast as an integral part of an implementation
100 of the GEFS at NOAA. In addition, North American Ensemble Forecast System (NAEFS;
101 Candille 2009; Candille et al. 2010) products have been updated based on the GEFSv12 Phase
102 2 reforecast.

103 The reforecast system configuration is summarized in Section 2. The reforecast dataset,
104 public access, and data corrections are introduced in Section 3. The statistical characteristics
105 of the raw forecasts are described in Section 4. In Section 5, an example of the reforecast
106 application is discussed. Summary and conclusions are given in Section 6.

107 **2. Reforecast system configuration**

108 The GEFSv12 reforecast system is based on the current operational Global Forecast
109 System version 15.1 (GFSv15.1; EMC website, 2019) which uses the Geophysical Fluid
110 Dynamics Laboratory (GFDL) FV3 Cubed-Sphere dynamical core (Lin and Rood 1997; Lin

111 2004; Putman and Lin 2007; Harris and Lin 2013). The resolution of the forecast system is ~25
112 km (C384 grid) in the horizontal with 64 vertical hybrid levels with the top layer centered
113 around 0.27 hPa (~55 km).

114 The convection scheme used in the GEFSv12 is the Simplified Arakawa-Schubert
115 (SAS) shallow and deep convection schemes (Han and Pan 2011) updated with a scale-aware
116 parameterization (Han et al. 2017). The scheme was also further modified to reduce excessive
117 cloud top cooling for the model stabilization. The cloud microphysics scheme is from GFDL,
118 which includes five predicted cloud species (cloud water, cloud ice, rain, snow and graupel;
119 Zhou et al. 2019, 2021). The vertical mixing process of the planetary boundary is based on the
120 hybrid Eddy-diffusivity Mass-flux (EDMF) scheme (Han et al. 2016). The shortwave and
121 longwave radiative fluxes are calculated using the rapid radiative transfer model (RRTM)
122 developed at Atmospheric and Environmental Research (Clough et al. 2005). The GFS
123 orographic gravity wave drag and mountain blocking schemes follows Alpert (1988), while
124 convective gravity wave drag employs the scheme developed by Chun and Baik (1998). The
125 GFS Noah land surface model (Chen et al., 1996; Koren et al. 1999; Ek et al. 2003; Michell et
126 al. 2005) are used to simulate the land-surface processes. The surface layer parameterization
127 follows Long (1984; 1986) and Zheng et al. (2012; 2017).

128 The SST boundary condition is derived from a two-tiered Sea Surface Temperature
129 (SST) and Near Sea Surface Temperature (NSST) approach that accounts for the day-to-day
130 variability and diurnal variation of SST, respectively (Zhu et al. 2017, 2018; Li et al. 2019). A
131 modern ensemble forecast system should include initial perturbations to approximate
132 analysis/observation uncertainty and model perturbations to approximate the forecast
133 uncertainty from model imperfections, such as the finite resolution of the prediction system
134 and the use of deterministic parameterizations of sub-grid phenomena (Buizza et al. 1999;
135 Palmer 2001, 2012; Berner et al. 2017). To improve the model's uncertainty representation,
136 stochastic kinetic energy backscatter (SKEB; Shutts and Palmer 2004; Shutts 2005) and
137 stochastically perturbed parameterization tendencies (SPPTs; Buizza et al. 1999; Palmer et al.
138 2009) are applied. More details on the GEFSv12 forecast system can be found in Zhou et
139 al. (2019; 2021).

140 The reforecast was integrated once per day out to 16 days, except on Wednesdays when
 141 the forecast was extended to 35 days. In contrast to the real-time forecast system (31 members),
 142 the reforecast system has a smaller ensemble size to minimize computational expense: 5 and
 143 11 members for the 16-day and 35-day runs, respectively. As illustrated in Table 1, the
 144 reforecast utilizes two sets of analysis data because a consistent 31-year reanalysis is
 145 unavailable.
 146

Reforecast characteristic	1989-1999	2000-2019
Reanalysis states for initial conditions	CFSR (Saha et al. 2010) + bred vectors (Wei et al. 2008)	GEFSv12 (Hamill et al. 2021)
SST initial states	OI (Reynolds et al. 2002)	OI (Reynolds et al. 2002)
SST forecast	NSST (Zhu et al. 2017, 2018; Li et al. 2019)	NSST (Zhu et al. 2017, 2018; Li et al. 2019)
Soil moisture and vegetation classification for initial states	Following Zobler 1986, 1999, Dorman and Sellers 1989).	Following Ek et al. (2016)

147
 148 **Table 1.** The summary of initial and boundary conditions for the GEFSv12 reforecasts.
 149

150 For the Phase 1 reforecast (GEFSv12_p1, 1989–1999), the Climate Forecast System
 151 Reanalysis (CFSR; Saha et al. 2010) was used as the initial control analysis. The breeding
 152 vector and ensemble transform with rescaling (BV-ETR) cycling perturbations (Wei et
 153 al. 2008), generated for the NOAA’s 2nd generation GEFS reforecast (Hamill et al., 2013),
 154 was used as initial conditions for the perturbed members. The new 16 State Soil Geographic
 155 (STATSGO) soil classification and 20 International Geosphere Biosphere Programme (IGBP)
 156 vegetation classification (Ek et al. 2016) were applied to characterize soil and vegetation in the
 157 reforecast runs, although the CFSR used the old 9 soil texture classes (Zobler 1986, 1999) and
 158 13 vegetation catalogues (Dorman and Sellers 1989).

159 For the Phase 2 reforecasts (GEFSv12_p2, 2000–2019), initial conditions were
160 GEFSv12 reanalyses (Hamill et al. 2021). The reanalyses were generated from the FV3
161 GFS/Ensemble Kalman Filter (EnKF) hybrid analyses and EnKF 6-h forecasts with the
162 Incremental Analysis Update (IAU; Bloom et al. 1996) replay process, which distributes the
163 analysis increments over each time step within a fixed time window (currently 2100–0300
164 UTC). During this replay procedure, the climatological snow depths at 0000, 0600, and 1200
165 UTC (affected by a bug in data assimilation, see Hamill et al. 2021) were replayed to
166 corresponding snow analyses to adjust reanalysis states to be more consistent with the snow
167 analyses at these times. The GEFSv12_p2 reforecast was initiated from the data at the end of
168 the replay IAU window (i.e., 0300 UTC). For both the GEFSv12 reanalysis and GEFSv12_p2
169 reforecast, soil moisture and vegetation were sorted based on the 16 soil-moisture and 20
170 vegetation types (Ek et al. 2016).

171 The GEFSv12 reanalysis also has several differences compared to the current
172 operational analysis. First, the IAU process was applied to reduce noise and improve accuracy.
173 Second, the NSST was replaced by Optimum Interpolation Sea Surface Temperature (OISST;
174 Reynolds et al. 2002) to avoid an observed large SST bias in climatologically cloudy regions
175 for the earlier assimilation years. Third, to reduce the computation resources required, the
176 horizontal resolutions of the control and perturbed members were decreased from C768 (~13
177 km) and C384 (~25 km) to C384 and C192 (~50 km), respectively. A detailed description of
178 the GEFSv12 reanalysis can be found in Hamill et al. (2021).

179 **3. Reforecast dataset, public access, and data corrections**

180 *a. Reforecast dataset and public access*

181 The full 31 years of reforecast data are currently archived on the High Performance
182 Storage System (HPSS). All 590 variables in grib2 format are saved at 3-hour intervals at 0.25°
183 resolution for the first 10 days and 6-hour intervals at 0.5° beyond 10 days of the forecast. By
184 request, 77 of the 590 variables were stored on the WCOSS disk for quick access by the internal
185 NOAA stakeholders. The 219 selected variables for the Phase 2 reforecasts are saved on
186 dedicated disks mounted on NOAA/NWS/NCEP's ftp server (
187 <ftp://ftp.emc.ncep.noaa.gov/GEFSv12/reforecast>) and Amazon Web Services (AWS,

188 <https://noaa-gefs-retrospective.s3.amazonaws.com/index.html>), which are accessible by the
 189 broader community. These 176 upper-air and 43 surface or single-level publicly accessible
 190 variables are separately listed in Tables 2 and 3, respectively. For pressure-level data above
 191 700 hPa (Table 2), the Phase 2 data are also saved at 0.5-degree grid spacing, even during the
 192 first 10 days of the forecast, to conserve space.

193

Vertical Level	U	V	W	T	Height (P)	Q (RH)	PV
1 hPa	X	X	X	X	X		
2 hPa	X	X	X	X	X		
3 hPa	X	X	X	X	X		
5 hPa	X	X	X	X	X		
10 hPa	X	X	X	X	X		
20 hPa	X	X	X	X	X		
30 hPa	X	X	X	X	X		
50 hPa	X	X	X	X	X		
70 hPa	X	X	X	X	X		
100 hPa	X	X	X	X	X	X	
150 hPa	X	X	X	X	X	X	
200 hPa	X	X	X	X	X	X	
250 hPa	X	X	X	X	X	X	
300 hPa	X	X	X	X	X	X	
400 hPa	X	X	X	X	X	X	
500 hPa	X	X	X	X	X	X	
600 hPa	X	X	X	X	X	X	
700 hPa	X	X	X	X	X	X	
800 hPa	X	X	X	X	X	X	
850 hPa	X	X	X	X	X	X	
900 hPa	X	X	X	X	X	X	
925 hPa	X	X	X	X	X	X	
950 hPa	X	X	X	X	X	X	
975 hPa	X	X	X	X	X	X	
1000 hPa	X	X	X	X	X	X	
1(hybrid)	X	X	X	X	X	(X)	
2(hybrid)	X	X	X	X	X	(X)	
3(hybrid)	X	X	X	X	X	(X)	
4(hybrid)	X	X	X	X	X	(X)	
2x10 ⁻⁶ (PV)	X	X		X	(X)		

310x10 ⁻⁶ Km ² kg ⁻¹ s ⁻¹ (Isentropic)							X
320x10 ⁻⁶ Km ² kg ⁻¹ s ⁻¹ (Isentropic)							X
350x10 ⁻⁶ Km ² kg ⁻¹ s ⁻¹ (Isentropic)							X
10m (AGL)	X	X					
100m (AGL)	X	X					

194

195 **Table 2.** One-hundred seventy-six upper air variables.

196

Variables	total
Mean sea-level pressure	1
Surface pressure	1
Surface height	1
Skin temperature	1
Soil temperature at 0.0-0.1, 0.1-0.4, 0.4-1.0 and 1.-2. m depth	4
Volumetric soil content at 0.0-0.1, 0.1-0.4, 0.4-1.0 and 1.-2. m depth	4
Water equivalent of accumulated snow depth	1
2-m temperature	1
2-m specific humidity	1
Maximum temperature in last 6-h period (00, 06, 12, 18 UTC) or in last 3-h period (03, 09, 15, 21 UTC)	1
Minimum temperature in last 6-h period (00, 06, 12, 18 UTC) or in last 3-h period (03, 09, 15, 21 UTC)	1
Surface wind gust	1
Surface wind stress, u-component	1
Surface wind stress, v-component	1
Surface roughness	1
Total precipitation in last 6-h period (00, 06, 12, 18 UTC) or in last 3-h period (03, 09, 15, 21 UTC)	1
Convective precipitation in last 6-h period (00, 06, 12, 18 UTC) or in last 3-h period (03, 09, 15, 21 UTC)	1
Non-convective precipitation in last 6-h period (00, 06, 12, 18 UTC) or in last 3-h period (03, 09, 15, 21 UTC)	1
Boundary layer height	1
Average surface latent heat net flux average in last 6-h period (00, 06, 12, 18 UTC) or in last 3-h period (03, 09, 15, 21 UTC)	1
Average surface sensible net heat flux average in last 6-h period (00, 06, 12, 18 UTC) or in last 3-h period (03, 09, 15, 21 UTC)	1
Average ground heat net flux average in last 6-h period (00, 06, 12, 18 UTC) or in last 3-h period (03, 09, 15, 21 UTC)	1
Convective available potential energy	1

Convective inhibition	1
0-3 km Storm relative helicity	1
Perceptible water	1
Total ozone	1
Total cloud cover average in last 6-h period (00, 06, 12, 18 UTC) or in last 3-h period (03, 09, 15, 21 UTC)	1
Downward shortwave radiation flux at the surface average in last 6-h period (00, 06, 12, 18 UTC) or in last 3-h period (03, 09, 15, 21 UTC)	1
Downward longwave radiation flux at the surface average in last 6-h period (00, 06, 12, 18 UTC) or in last 3-h period (03, 09, 15, 21 UTC)	1
Upward shortwave radiation flux at the surface average in last 6-h period (00, 06, 12, 18 UTC) or in last 3-h period (03, 09, 15, 21 UTC)	1
Upward longwave radiation flux at the surface average in last 6-h period (00, 06, 12, 18 UTC) or in last 3-h period (03, 09, 15, 21 UTC)	1
Upward longwave radiation flux at the top of the atmosphere average in last 6-h period (00, 06, 12, 18 UTC) or in last 3-h period (03, 09, 15, 21 UTC)	1
Momentum Flux, U-Component Average in last 6-h period (00, 06, 12, 18 UTC) or in last 3-h period (03, 09, 15, 21 UTC)	1
Momentum Flux, V-Component average in last 6-h period (00, 06, 12, 18 UTC) or in last 3-h period (03, 09, 15, 21 UTC)	1
Cloud ceiling	1
Water runoff sum over the last 6-h period (00, 06, 12, 18 UTC) or in last 3-h period (03, 09, 15, 21 UTC)	1

197

198 **Table 3.** Forty-three surface and other single-level variables.

199

200 *b. Data corrections*

201 The integrations for the Phase 2 reforecasts were initiated from the 0300 UTC restart
202 data files. Thus, the model outputs for the 41 0000-0300 UTC and 0000-0600 UTC
203 accumulated / minimum / maximum / average variables are incorrect since they were actually
204 calculated based on the values from the beginning of integration (i.e., 0300 UTC) to the first
205 time-step and to 0600 UTC, respectively. These 41 variables were post-processed by
206 combining the control NEMSIO (NOAA Environmental Modeling System Input/Output)
207 replay reanalysis at 0300 UTC and the reforecast data at 0600 UTC. Note that the replay
208 process was only applied to the control members so that for 0300 UTC, the reforecast data for
209 each member was simply replaced by the corresponding control-member replay data. For 0600
210 UTC, the minimum and maximum are the smaller and larger of the two values, respectively,
211 while the accumulated values are the sum of the two. The 6-h average fields were processed in

212 a more complicated manner. The raw reforecast average field at 0600 UTC is actually the
213 0300–0600 UTC accumulation divided by a 6-h time period, while in reality the accumulations
214 take place over a 3-h period. This was corrected to a 3-h average and then averaged with the
215 reanalysis data at 0300 UTC. But for some variables and conditions such an average is not
216 suitable and special processing is needed. For cloud-base/cloud-top pressures and cloud-top
217 temperatures, the 0000–0600 averages were set to be the same as those at 0300 UTC when
218 clouds do not exist in the 0600 UTC, while the corresponding averages were set to be the same
219 as those at 0600 UTC when clouds do not present in the 0300 UTC forecasts. Such a special
220 rule was also applied to snow melting flux.

221 **4. Reforecast evaluation**

222 In addition to the GEFSv12 reforecast and corresponding reanalyses used for
223 initialization described in Section 3, there are also six sets of additional data being used for the
224 current evaluations and comparisons. These additional datasets are as follows:

225 1. CFS reanalysis (1979–Mar 2011) at T382L64 (~34 km horizontal) resolution. The
226 documentation of the system, including the configurations, can be found in Saha et al. 2010.
227 The dataset was used as the initial condition for NOAA's second-generation of reforecasts (or
228 GEFSv10 reforecast; Hamill et al. 2013) and GEFS_SubX reforecast (Zhu et al. 2018).

229 2. NCEP's operational analysis from the GDAS (NCEP hybrid Global Data Assimilation
230 System) (2011–Present). The documentation of the GDAS upgrade, including the changes in
231 configurations, can be tracked through the EMC web-page:
232 https://www.emc.ncep.noaa.gov/emc/pages/numerical_forecast_systems/gfs.php

233 These data served as the initial condition for the GEFSv10 and GEFS_SubX reforecasts for the
234 periods 2011–present and 2011–2016, respectively.

235 3. The European Centre for Medium-Range Weather Forecasts (ECMWF) reanalysis
236 version 5 (ERA5) (1950–Present) data approximately 30 km horizontal resolution with 137
237 hybrid vertical levels, up to an 80 km model top. The documentation of the ERA5 system,
238 including the configurations, can be found through ECMWF's web-page:
239 <https://confluence.ecmwf.int/display/CKB/ERA5%3A+data+documentation>. These data were
240 used to evaluate the 2-m temperature forecast for the GEFSv12 and GEFS_SubX reforecast.

241 4. NCEP’s Climate Calibrated Precipitation Analysis (CCPA; 2002–Present) version 4
242 (v4) for Continental United States (CONUS). The documentation can be found in Hou et al.
243 (2014) and Luo et al. (2018). These data were used to evaluate precipitation forecasts for the
244 GEFS_SubX and GEFSv12 reforecasts and to calibrate the GEFSv12 reforecast.

245 5. GEFSv10 reforecast (1985–2011) and forecast (2012–2019). The documentation on
246 this system and configurations can be found through Zhu et al. (2012) and Hamill et al. (2013).
247 These data were used for the comparison with the GEFSv12 reforecast for hurricane track
248 forecasts.

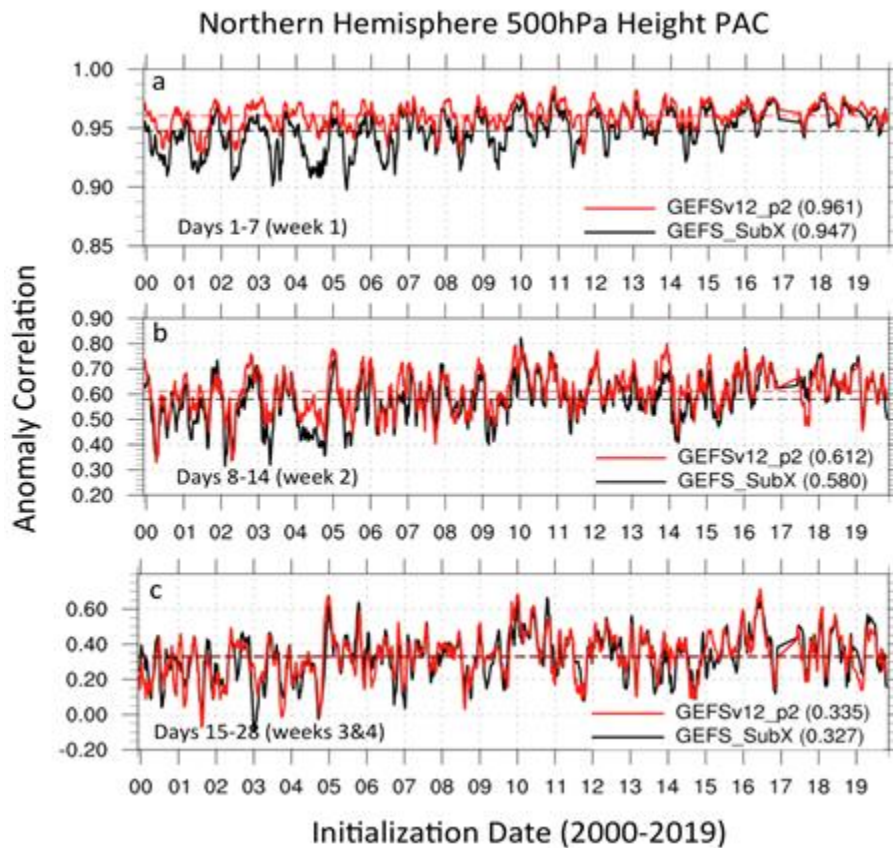
249 6. GEFS_SubX reforecast (1999–2016) and forecast (2017–2018) at TL574L64 (day 0–
250 8; ~34 km horizontal resolution) and TL382L64 (day 8–35; ~52 km horizontal resolution). The
251 documentation of the GEFS_SubX system and the configurations can be found in Zhu et al.
252 (2018). The GEFS_SubX reforecast is considered a benchmark dataset to measure the ability
253 of the GEFSv12 reforecast to predict 500-mb geopotential height, 2-m temperature,
254 precipitation, and Madden Julian Oscillation (MJO).

255 *a. 500-hPa geopotential height*

256 The anomaly correlation of 500-hPa geopotential height is widely used as an essential
257 metric to estimate the skill of weather forecasts, especially for mid- and high-latitude weather
258 systems. Here, 500-hPa geopotential height for the GEFS_SubX and GEFSv12_p2 reforecasts
259 are evaluated against their own analyses (i.e., CFSR and GEFSv12 reanalysis). CDAS2 is the
260 analysis climatology used to calculate analysis anomalies as well as forecast anomalies for
261 both GEFSv12_p2 and GEFS_SubX. Over the Northern Hemisphere (NH, Fig. 1), the
262 GEFSv12_p2 outperforms the GEFS_SubX with improvements in average anomaly
263 correlation (AC) of 1.5%, 5.5%, and 2.5% for week 1, week 2, and weeks 3 and 4 forecasts,
264 respectively. Like Zhu et al.’s work (2018), the anomaly correlations for week 1, week 2,
265 and weeks 3 and 4 are calculated by averaging forecast lead days 1–7, 8–14, and
266 15–28, respectively, and the corresponding analysis valid at 0000 and 0012 UTC.
267 Over the Southern Hemisphere (SH, Fig. 2), the average AC scores are slightly lower than over
268 the NH, which is consistent with the previous finding in Zhu et al. (2018) for the evaluation of
269 the 16-year GEFS_SubX reforecast. Relative to the GEFS_SubX, the GEFSv12_p2 shows

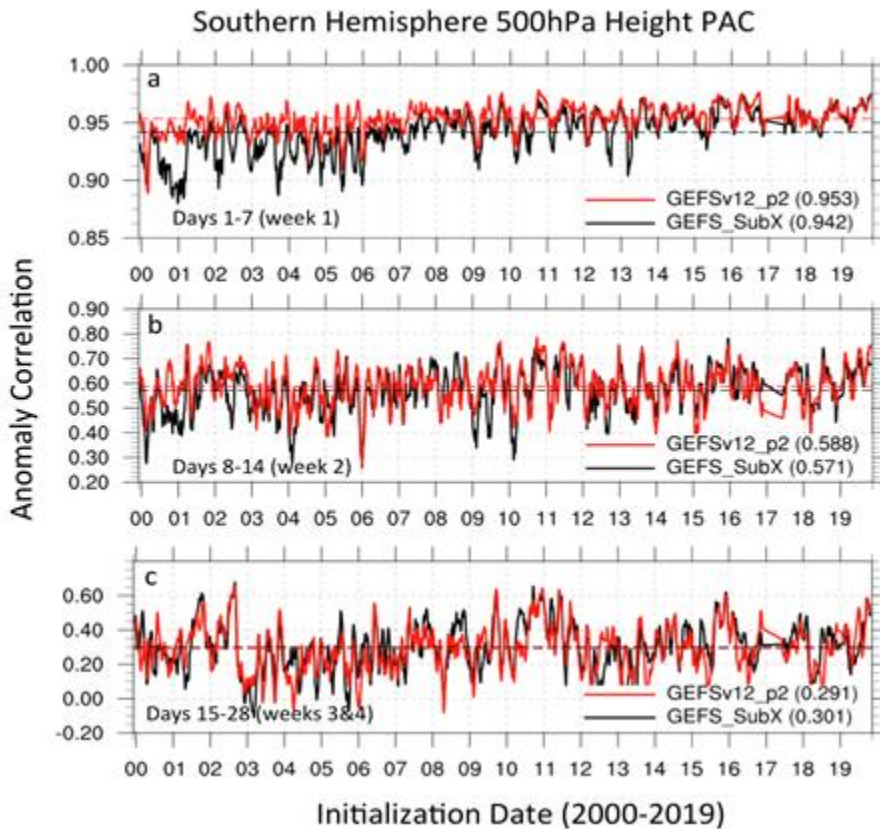
270 1.3% and 3.0% improvements for week 1 and week 2 forecasts and a 3.3% degradation for the
 271 weeks 3 and 4 forecasts. The significant tests indicate that the Week -1 and Week-2
 272 GEFSv12_p2 AC are significantly higher than GEFS_SubX for both NH and SH, while the
 273 corresponding AC values are not significantly different between the GEFSv12_p2 and
 274 GEFS_SubX for Weeks 3 and 4. The figures also reveal higher AC scores in the second decade
 275 (2010–2019) than the first decade (2000–2009) of the reforecast, and the corresponding
 276 calculations indicate that the weeks 3 and 4 scores for the NH in the second decade increase
 277 by 0.074 (or 25%) and 0.077 (or 26%) for the GEFS_SubX and GEFSv12_p2, respectively.
 278 The enhanced observation system (Noh et. al. 2020) may be an explanation for the better
 279 performances of 500-hpa forecasts in the most recent decade.

280



281
 282 Figure 1. Ensemble-mean anomaly correlation for Northern Hemisphere (NH; 20°N–80°N)
 283 500-hPa geopotential height for week 1 (a), week 2 (b), and weeks 3&4 (c) forecasts. The black
 284 and red colors denote the GEFS_SubX and GEFSv12_p2. The average scores for the two sets
 285 of reforecasts are indicated by the dashed lines and shown in parentheses. Note there is a data

286 gap from Dec 2016 to May 2017, corresponding to the period between the GEFS_SubX
 287 reforecast and corresponding real-time forecast. A 6-case moving average is applied to the time
 288 series. Since the forecasts are initialized every 7 days, the moving average spans over 42
 289 calendar days.
 290



291
 292 Figure 2. The same as Fig. 3 except for the Southern Hemisphere (SH; 20°S–80°S).

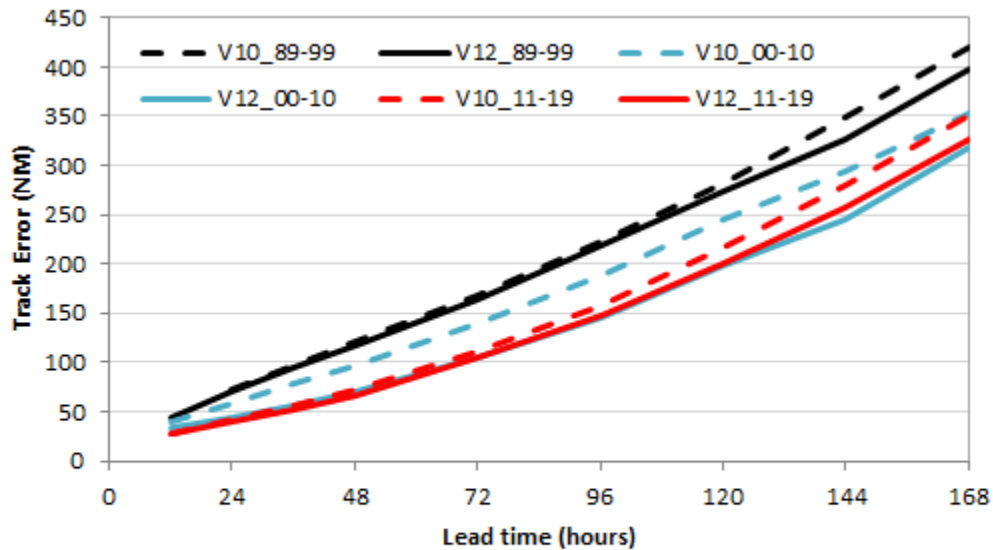
293
 294 *b. Tropical cyclone track*

295 Tropical cyclone (TC) track forecasting has been challenging (Landsea and Cangialosi
 296 2018), especially for the extended range (beyond day 5). To evaluate the ability of GEFSv12
 297 to forecast tracks, track errors of the 5-member ensemble means of the GEFSv10 and GEFSv12
 298 are compared for the 31-year reforecast period. The GEFSv10 was selected because it has a
 299 large sample data size like the GEFSv12 does. For consistency, in addition to the 5-member
 300 runs of the GEFSv12 reforecast, only the first five members of the GEFSv10 and of the 11-
 301 member runs of GEFSv12 are used in this comparison. The National Hurricane Center

302 (NHC)/Joint Typhoon Warning Center (JTWC) best (or observed) tracks were used as a
303 reference for evaluating the two datasets.

304 The GEFSv12 skill in forecasting TC tracks has improved from the GEFSv10. Figure
305 3 shows the three-basin (Atlantic, East Pacific and West Pacific) averaged track errors from
306 both forecast systems, binned by decade. For all three decades, the GEFSv12 reduces the track
307 errors with the maximum reduction during the 2000-2010 period, when the reductions reach
308 approximately 25% and 10% for 1-day and 7-day forecasts, respectively. For the GEFSv10,
309 the track errors decline with decade (Fig. 3), which is qualitatively consistent with the finding
310 in Hamill et al. (2013), based on the 1985-2011 reforecast. This evolution of the track errors is
311 attributed to the improvement in the initial analysis over the multi-decade period, implying the
312 important impact of initial conditions on the TC track forecast. For the shorter lead times, the
313 decline in error from the 2000–2010 to 2011–2019 period is more evident than that from the
314 1989–1999 to 2000–2010 period. For example, the error reduction is 11.6 nm (or 29.8%)
315 between the two later periods, while the corresponding reduction is 5.7 nm (or 12.8%) between
316 the two earlier periods. In addition to the observation data increase with decade, the analysis
317 system upgrade from CFSR to GFS/GDAS and the perturbation method change from BV-ETR
318 to EnKF during the 2011–2019 period may be a reason for the observed sharper error reduction.
319 The impact of initial conditions is also further confirmed in the current GEFSv12 reforecast.
320 The track errors in the two GEFSv12 reanalysis time periods (2000–2010 and 2011–2019) are
321 more consistent with each other and much smaller compared to the CFSR period (1989–1999),
322 showing the importance of initialization with modern assimilation methods. The consistent
323 error characteristics during the Phase 2 reforecast provide a good potential for statistical post
324 processing algorithms to improve the TC track forecast (Galarneau and Hamill 2015). In
325 addition to the initial conditions, the reforecast model itself also plays a role in influencing the
326 accuracy of the track forecast. This is illustrated by the comparison between the GEFSv10 and
327 GEFSv12 during the 1989–1999 period, when both reforecasts used the CFSR as the initial
328 condition. As should be expected, the model’s influence becomes more pronounced at longer
329 lead times (> ~4-days). Compared to GEFSv10, the GEFSv12 reduces the track errors by 6.3%
330 and 5.5% for the 6-day and 7-day forecasts, respectively.

331
332
333
334

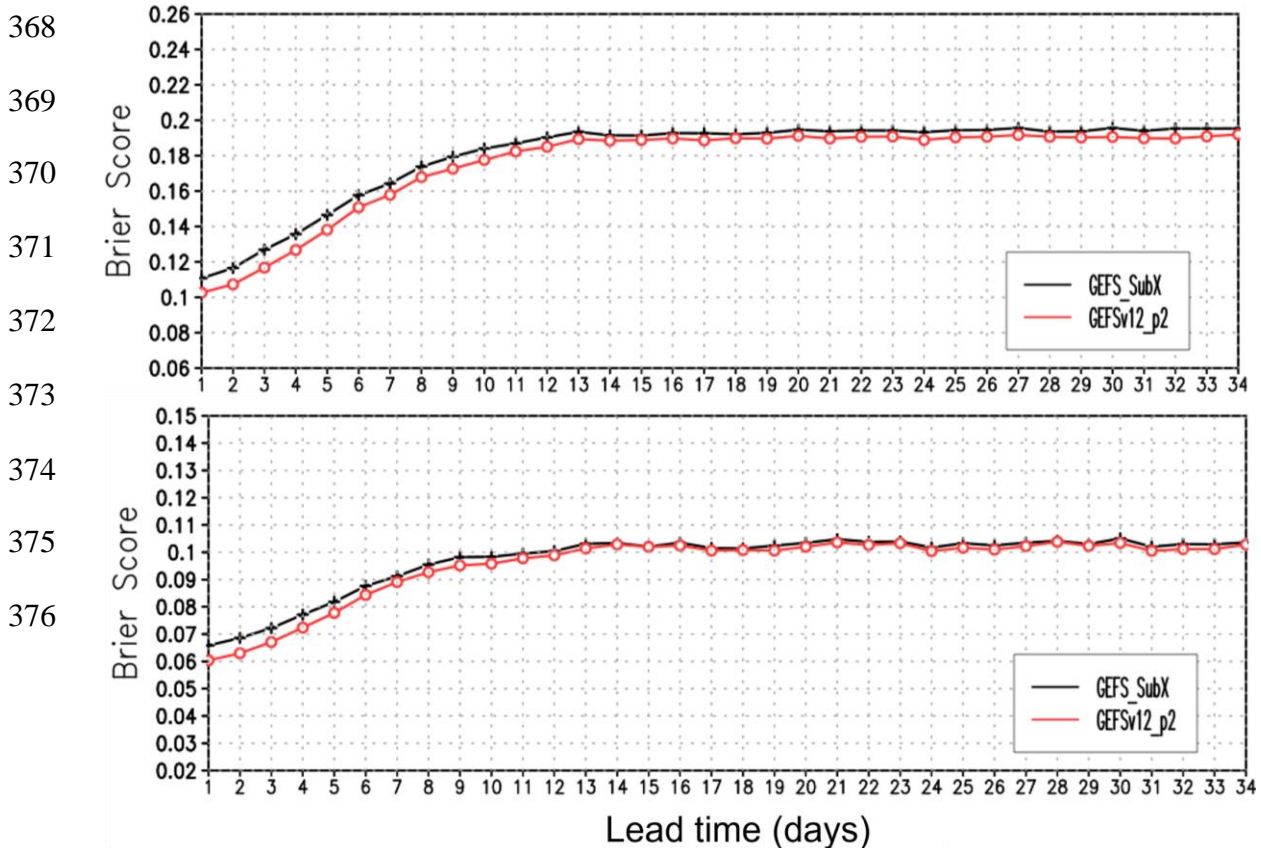


335
336 Figure 3. The TC track errors averaged over the Atlantic, East Pacific and West Pacific basins
337 binned by decade during the 31-year reforecast for GEFSv10 (dashed lines) and GEFSv12
338 (solid lines). Black, blue, and red lines denote the 1989–1999, 2000–2010, and 2011–2019
339 periods, respectively.
340

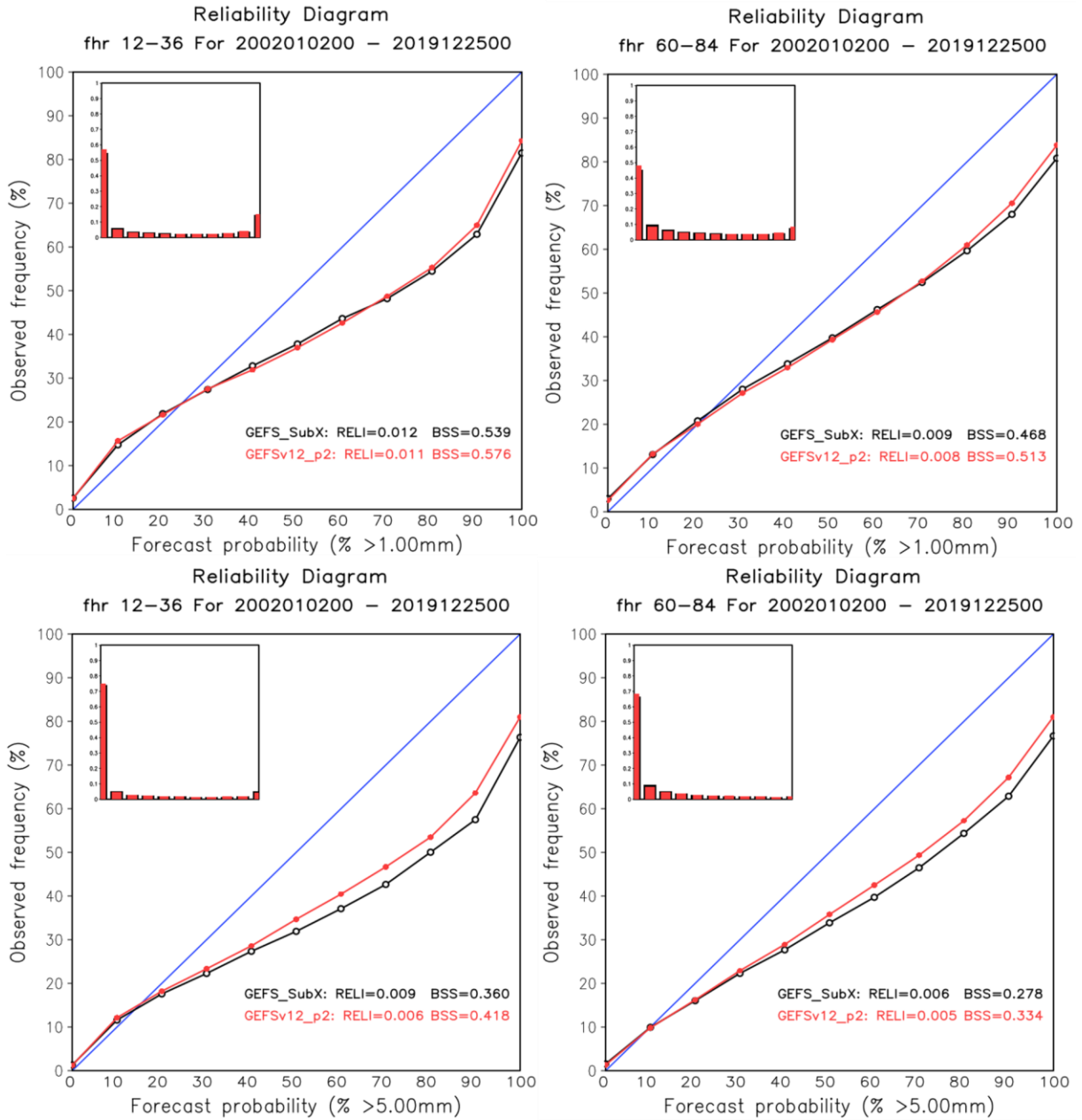
341 *c. Precipitation*

342 The precipitation forecasts for the GEFS_Subx and GEFSv12 were estimated against
343 the CCPAv4 for the 2002–2019 period when the reforecast and CCPA data overlapped. The
344 CCPA climatology was calculated based on the 2002-2019 CCPA data. For this study, the 11-
345 member reforecasts and CCPA data were interpolated to a 1°x1° grid over the Continental
346 United States (CONUS), the only available analysis region. Figures 4a and 4b show the
347 comparisons of Brier score (BS, Brier 1950) between the two sets of reforecasts for the 24-h
348 accumulated precipitation greater than 1 mm and 5 mm, respectively. The BS, ranging between
349 0 and 1, is commonly used to verify the accuracy of a probability forecast. Clearly, the

350 GEFSv12 consistently displays the better (i.e., lower) Brier scores compared to the
 351 GEFS_SubX, with a more obvious improvement at lead times shorter than about 10 days.
 352 Forecast skill decreases with lead time and reaches saturated values at approximately day 13
 353 for all situations. The precipitation probability forecast biases for 12–36 hrs and 60–84 hrs for
 354 amounts greater than 1-mm and 5-mm were measured by reliability diagrams (Fig. 5). The
 355 GEFSv12 and GEFS_SubX show very similar performance for the precipitation greater than
 356 1.00 mm. For the heavier precipitation category (> 5 mm), the GEFSv12 slightly outperforms
 357 the GEFS_SubX with its curves being closer to the diagonal lines. Fig. 5 also shows the
 358 reliability curves are much closer to the diagonal at low probabilities but veering away for high
 359 probabilities. The Brier Skill Score (BSS, Wilks 1995) measures the improvement of the
 360 probability forecast over the reference climatology. Unlike BS, where lower is better, for BSS
 361 higher is better. In the heavier rain conditions, the BSS for the probabilistic precipitation
 362 forecast for the GEFSv12 are improved by about 16.1% and 20.1% for 12–36 hrs and 60–84
 363 hrs, respectively (Fig. 5). The improvements are also observed for the other lead times (not
 364 shown). These improvements are attributed to the combined influence of better initial
 365 conditions, more advanced microphysics schemes, finer resolution and a new FV3 dynamic
 366 core. The impact that each of these factors has individually on the evaluation is not addressed
 367 in this study.



377 Figure 4. The daily average Brier Score of the CONUS probabilistic quantitative
378 precipitation forecast (PQPF) from 2002 to 2019 for 24-h accumulated precipitation greater
379 than or equal to 1.00mm (top) and 5.00mm (bottom). The comparison is for the
380 GEFS_SubX reforecast (black) and GEFSv12_p2 reforecast (red) that were run once per
381 week (Wednesday) with 11 members out to 35 days. The reference truth is CCPAv4.



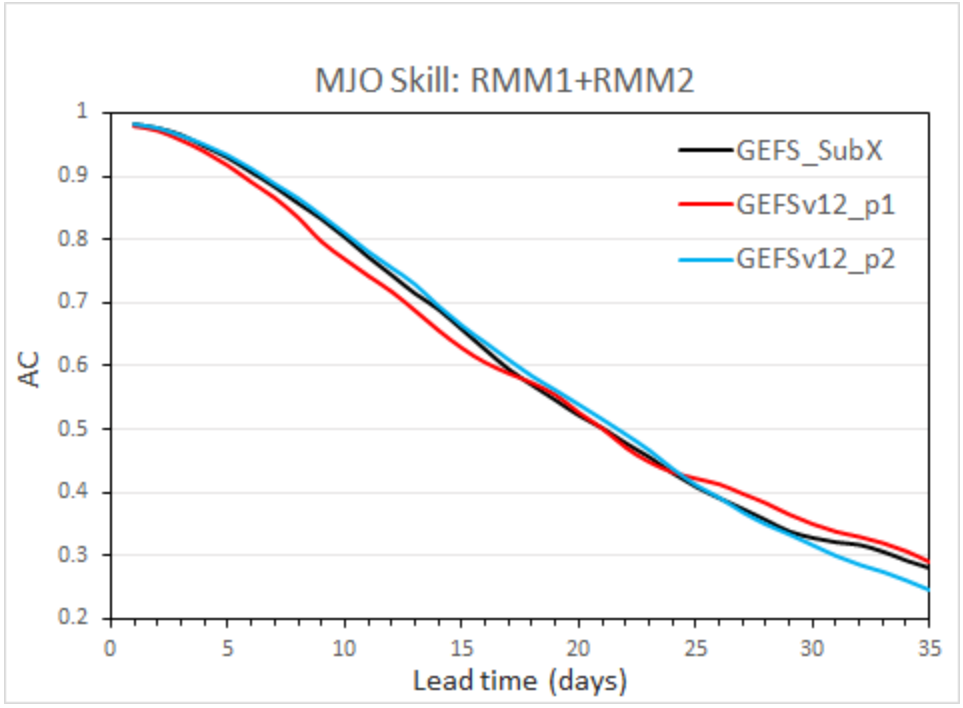
382
383
384
385
386
387
388
389
390
391

Figure 5. The reliability diagram of the CONUS probabilistic quantitative precipitation forecast (PQPF) from 2002 to 2019 for 24-h accumulated precipitation greater than or equal to 1.00mm (12-36 hours, top left; 60-84 hours, top right) and 5.00mm (12-36 hours, bottom left; 60-84 hours, bottom right). The comparison is for the GEFS SubX version reforecast (black) and GEFSv12_p2 reforecast (red) that run once per week (Wednesday) with 11 members out to 35 days. The reference truth is CCPAv4. The average reliability score (RELI) and Brier skill score (BSS) are also presented in each subplot. (Note: This is for a raw ensemble forecast with limited ensemble members (11) compared to the operational 31 members.)

392 *d. MJO prediction skill*

393 The newly operational GEFSv12 extended its output to +35 days lead to cover the sub-
394 seasonal time scale. The MJO is one of the most important climate phenomena for sub-seasonal
395 forecasts. Here we estimate MJO prediction skill using the real-time multivariate MJO (RMM)
396 index (Wheeler and Hendon 2004) for the GEFS_SubX, GEFSv12_p1, and GEFSv12_p2 (Fig.
397 6). Skill is defined as the bivariate anomaly correlation between the analysis and forecast
398 RMM1 and RMM2 index. For this comparison, the CFSR (GEFSv12 reanalysis) serves as the
399 reference analysis for the GEFS_SubX and GEFSv12_p1 (GEFSv12_p2). In other words, the
400 estimates are based on their own analysis data. Overall, the MJO forecast skill for the
401 GEFSv12_p2 (~21.5 days) is similar to the GEFS_SubX and GEFSv12_p1 (~21 days) when
402 using $AC=0.5$ as the threshold of useful skill. The SubX forecast skill for the 20-year sample
403 in this study is also very comparable to the estimate (~21–22 days) that was made using a much
404 smaller sample size (2 years) in Zhu et al. (2018) and Li et al. (2019). The GEFSv12_p2 also
405 exhibits higher skill for shorter lead times ($< \sim 18$ days) than the GEFSv12_p1, possibly due to
406 the benefit of the improved initial conditions for the Phase 2 reforecast. For lead times longer
407 than 22 days, the forecast skill for all three sets of data is poor. A fully coupled atmosphere-
408 ocean-wave-ice model, currently under development at NCEP, aims to improve the MJO
409 forecast skill, especially for longer lead times. The reader is referred to Hamill and Kiladis
410 (2013) for MJO verification on GEFSv10 reforecasts.

411



412
 413
 414
 415
 416
 417
 418

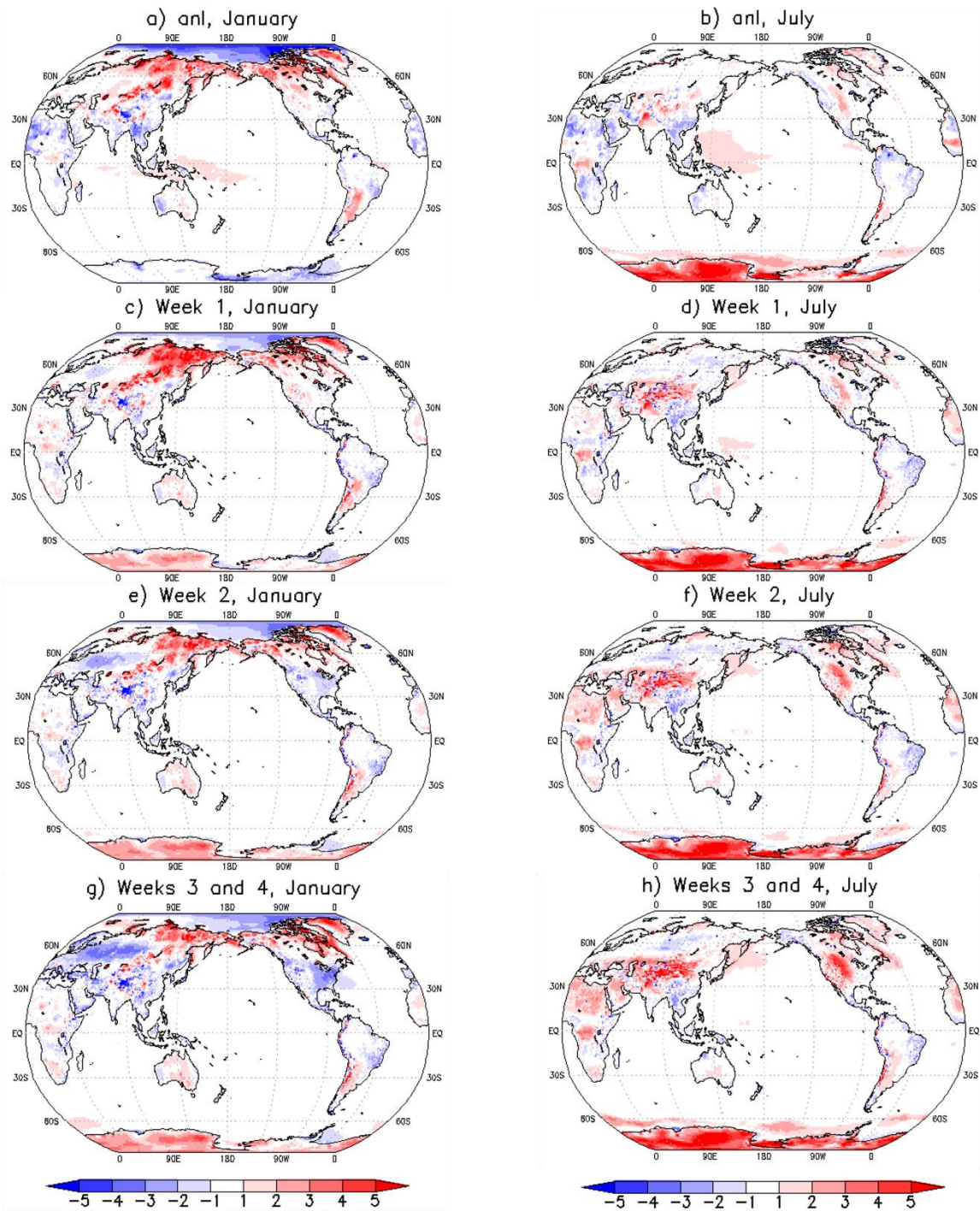
Figure 6. The real-time multivariate MJO (RMM) skill as a function of lead time for GEFS_SubX (black; 2000–2016), GEFSv12_p1 (red; 1989–1999), and GEFSv12_p2 (blue; 2000–2019) reforecasts.

e. 2-meter temperature errors

419
 420
 421
 422
 423
 424
 425
 426
 427
 428
 429
 430

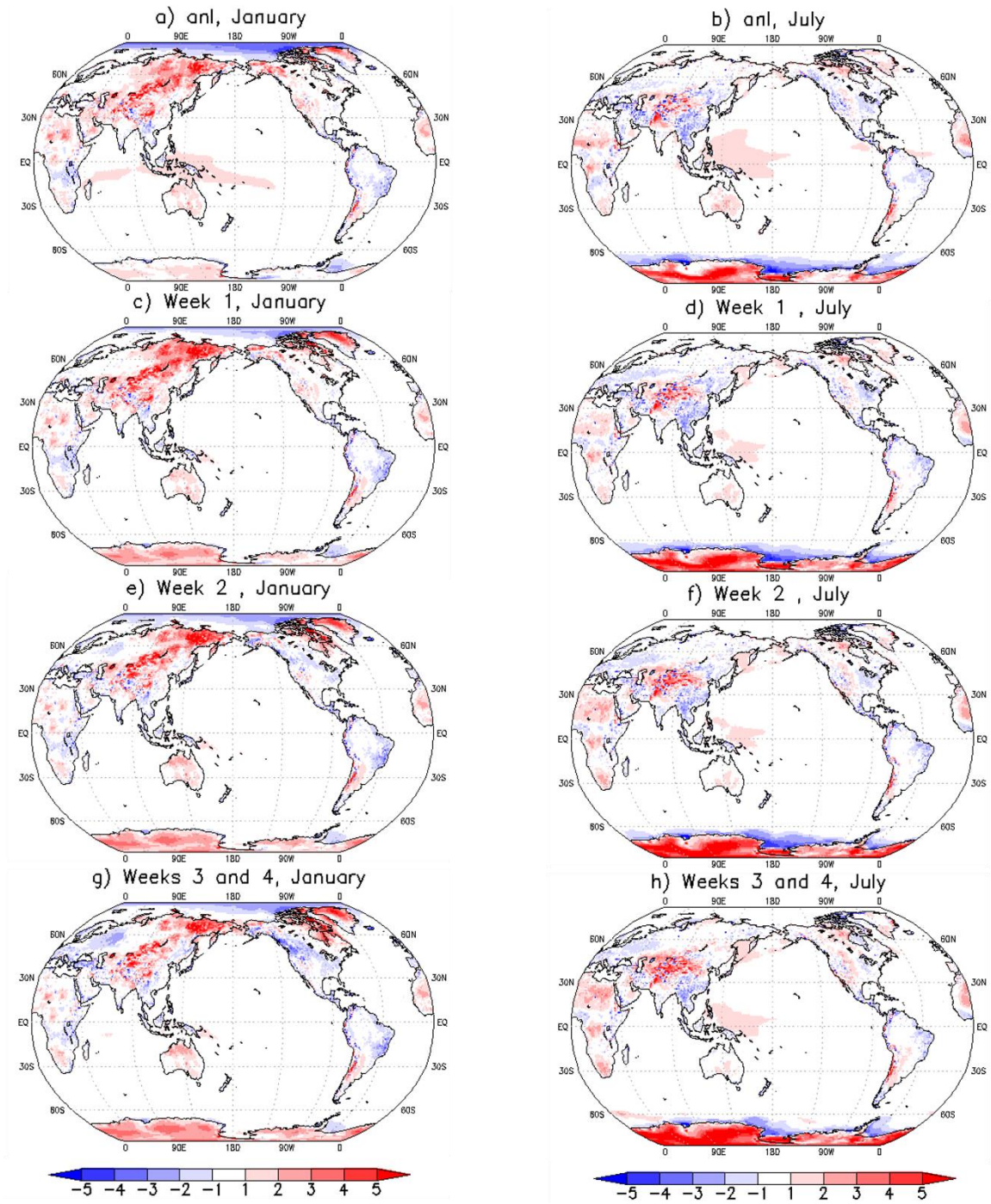
The January and July global 2-m temperature mean errors (or biases) for the 11-member runs were calculated for week 1, week 2, and weeks 3 and 4 during the GEFSv12_p1 (Fig. 7) and GEFSv12_p2 (Fig. 8) reforecast periods. The biases of week 1, week 2, and weeks 3 and 4 are the day 1–7, 8–14, and 15–28 averaged forecast errors over the corresponding forecast periods, respectively. Also displayed are the differences between CFSR and ERA5 (Fig. 7 a, b) and the differences between the GEFSv12 reanalysis and ERA5 (Fig. 8 a,b). The ERA5 was used as the reference for both phases to ensure a consistent comparison. A large warm bias over northern Asia is persistently seen in January (Figs. 7 a, c, e, and f and Figs. 8 a, c, e, and f) with a decreasing trend over increasing forecast lead time. In general, the error in 2-m temperature at the weeks 3 and 4 timescale is nearly saturated (Guan et al. 2019) and the impact from initial conditions decreases. At this timescale, the GEFSv12 generates a cold bias over North America (NA) in January (Figs. 7 g and 8 g). The cold bias locations are

431 different, mostly over the eastern United States for GEFSv12_p1 and western Canada for
432 GEFSv12_p2. A larger cold bias for the boreal winter season over the NA domain has been
433 persistently observed in several generations of the NCEP GEFS (Guan et al. 2015, 2019) and
434 was thought to be related to the imperfect parameterization of winter-associated physical
435 processes (Guan et al. 2019).
436



437
 438
 439
 440
 441
 442

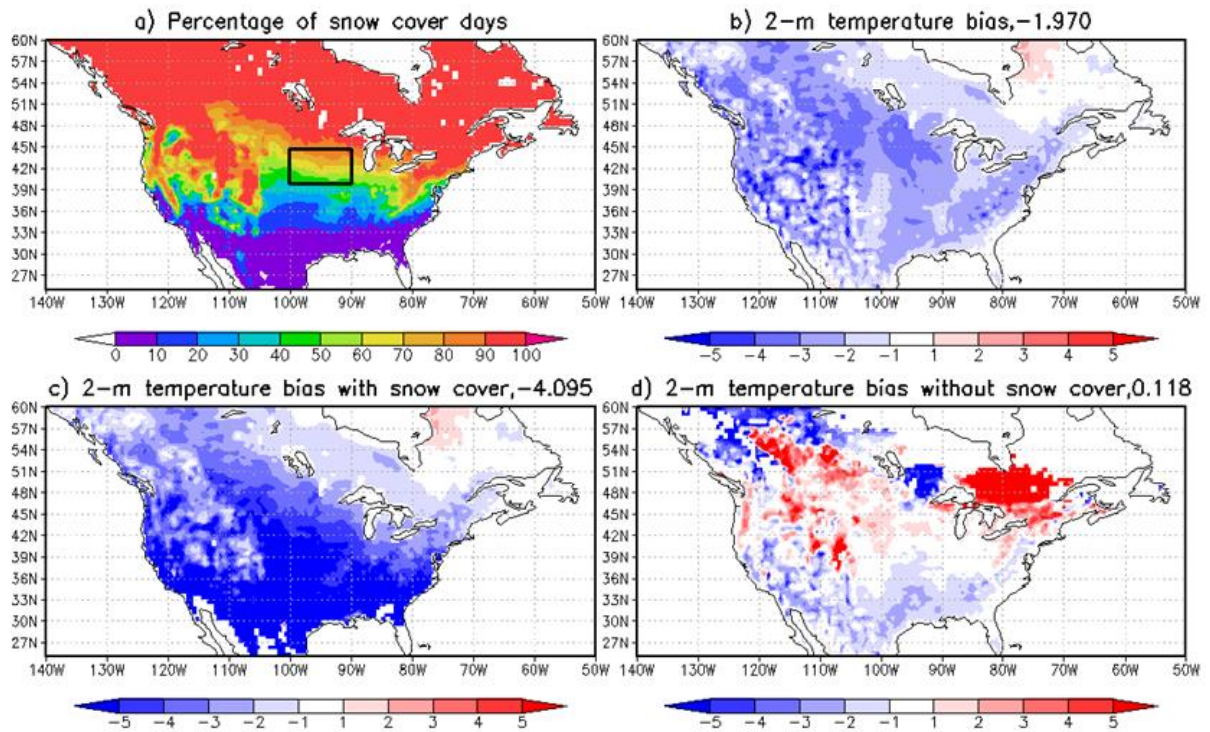
Figure 7. The difference in 2-m temperature ($^{\circ}\text{C}$) between the CFSR and ERA5 for January (a) and July (b) over phase 1. Spatial distribution of 2-m temperature mean error (i.e., bias) over phase 1 for January during (c) week 1, (e) week 2, and (h) weeks 3 and 4 forecasts, and July during (d) week 1, (f) week 2, and (g) weeks 3 and 4 forecasts.



443
 444
 445
 446
 447
 448
 449

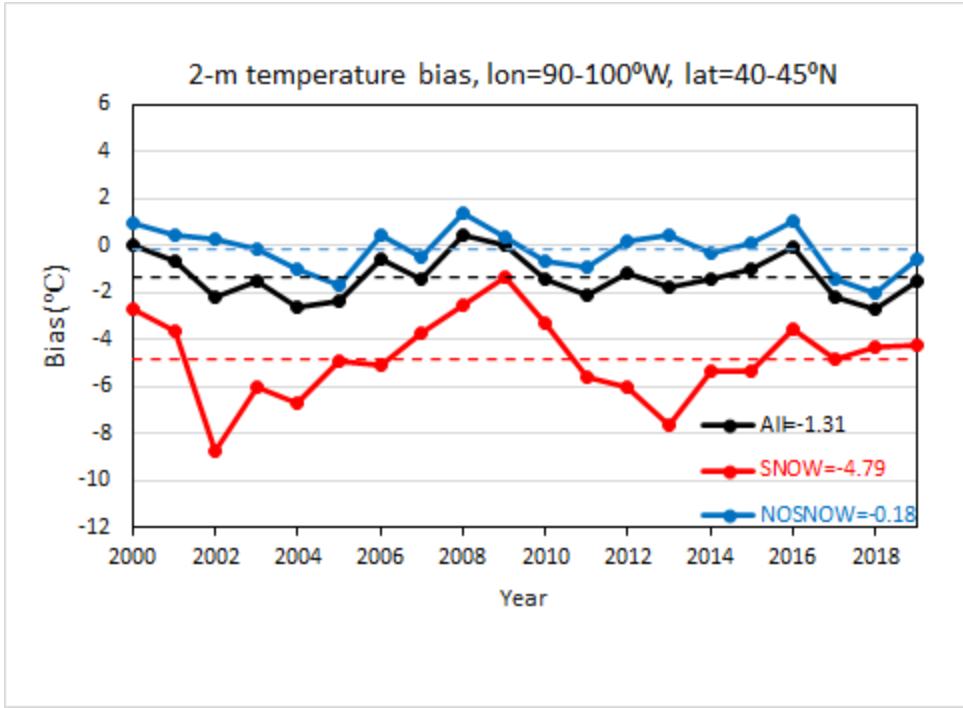
Figure 8. The difference in 2-m temperature ($^{\circ}\text{C}$) between the GEFSv12 reanalysis and ERA5 for January (a) and July (b) over phase 2. Spatial distribution of 2-m temperature mean error (i.e., bias) over phase 2 for January during (c) week 1, (e) week 2, and (h) weeks 3 and 4 forecasts, and July during (d) week 1, (f) week 2, and (g) weeks 3 and 4 forecasts.

450 Snow is considered to be one of the most important wintertime land surface
451 characteristics. To illustrate the influence of the snow forecast on bias characteristics, we
452 compare the 2-m temperature bias over the NA domain for the 408h forecast (approximately
453 the middle of week 3) with snow cover, without snow cover, and for all conditions (Fig. 9).
454 The comparison was performed based on control members for the GEFsv12_p2 reforecast
455 period. January–March is selected because those months show a consistently large cold bias
456 (see red line in Fig.10) and the expected frequent occurrences of snow cover. The selection by
457 individual members leads to a clear division between snow-covered and snow-free cases. The
458 existence of forecast snow was inferred if the snow water equivalent is greater than or equal to
459 1mm. Clearly, the 2-m temperature bias characteristics are quite different between the two
460 conditions (Fig. 9c and d). Figure 10 shows the time evolution of biases over a small region
461 near the central US. A larger cold bias is dominant under the existence of snow cover with a
462 domain-averaged value of -4.79°C during the GEFsv12_p2 period. In contrast, bias is much
463 smaller under snow-free conditions where the average value is about -0.18°C . This indicates
464 there is considerable room for improving the 2-m temperature forecast under snow-covered
465 conditions. An improvement in modeling snow-associated physical processes would
466 undoubtedly lead to a better 2-m temperature forecast. The large difference in bias
467 characteristics between cases with and without snow cover also suggests that statistical
468 calibration of 2-m temperature should be performed based on the existence of snow. It was
469 noted that the bias correction using a unified 2-m temperature bias climatology for the NA cold
470 season is much less efficient compared to the warm season (Guan et al., 2019). Apparently,
471 the proposed snow dependent bias correction method should improve statistical post
472 processing for the 2-m temperature forecast during the cold season. This will be confirmed in
473 our future work.
474
475



476
 477
 478
 479
 480
 481
 482
 483

Figure 9. Percentage of snow cover days (a), 2-m temperature forecast bias under all conditions (b), bias with snow cover forecast (c), bias without snow cover forecast (d) for 408-h control-member forecast over NA. The results are based on the GEFSv12_p2 reforecast for January, February, and March.



484

485

486 Figure 10. Time series of 2-m temperature forecast errors for 408-h control-member forecast
 487 over a small region (40°N-45°N, 90°W-100°W) near the central US (marked with the black
 488 rectangle in Fig. 9a). Black, red, and blue solid curves indicate the errors for January, February,
 489 and March forecasts under all conditions, with, and without snow cover, respectively. The
 490 corresponding dashed lines denote the averages over the entire period.

491

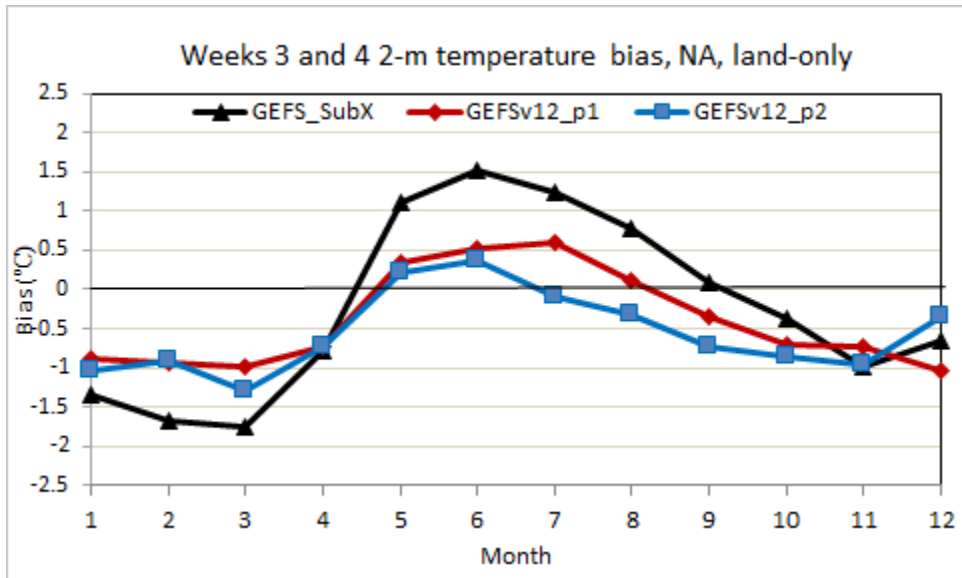
492 In contrast to January 2-m temperature biases in the initial state are relatively smaller
 493 in July (Figs. 7b and Figs. 8b). For weeks 3 and 4, the model showed a large warm bias over
 494 the central United States (US) during the GEFSv12_p1, which is consistent with the findings
 495 in Guan et al. (2019) though an earlier forecast system (i.e., GEFS_SubX) was used in that
 496 study. During the GEFSv12_p2, the model shows a bias pattern similar to the GEFSv12_p1,
 497 but the warm bias over the central US is reduced.

498

499 To better understand the impact of using different initial conditions and forecast
 systems to produce 2-m temperature forecasts, the seasonal variability of 2-m temperature bias
 500 is compared for the NA weeks 3 and 4 forecasts (land only) among the GEFS_SubX,
 501 GEFSv12_p1, and GEFSv12_p2 in Fig. 11. All three sets of reforecasts display a cold bias
 502 during the October-April and warm bias during the May-June period. The GEFS_SubX shows

503 the strongest seasonal variability (or largest amplitudes) with a maximum cold bias of -1.8°C
 504 in March and warm bias of 1.5°C in June. When the forecast systems are the same (i.e.,
 505 GEFSv12_p1 and GEFSv12_p2), the differences in 2-m temperature bias are relatively small.
 506 Overall, the GEFSv12_p1 is warmer than the GEFSv12_p2, except in December. The
 507 systematic difference during the July-September period is also noteworthy. Further diagnosis
 508 is needed to address this difference in the future.

509



510

511

512 Figure 11. Weeks 3 and 4 biases in 2-m temperature forecasts averaged during the GEFS_SubX
 513 (black, 1999–2016), GEFSv12_p1 (red, 1989–1999), and GEFSv12_p2 (blue, 2000–2019)
 514 reforecast periods over NA, land-only.

515

516 5. Post-processing of reforecast (precipitation)

517 Calibration is one of the most common applications of a reforecast dataset.
 518 Precipitation is one of the most impactful weather elements (Hamill and Whitaker 2006;
 519 Hamill et al. 2008; Hamill 2012; Schmeits and Kok 2010; Hamill et al. 2015; Hamill and
 520 Scheuerer 2018; Scheuerer and Hamill 2018; Specq and Batté 2020). Here we demonstrate the
 521 impact of using reforecast data to improve precipitation forecasts.

522 a Methodology

523 We take advantage of long-term training data to calibrate precipitation through a
524 quantile-mapping technique (Ines and Hansen 2006; Hamill and Scheuerer 2018). A ‘quantile-
525 based’ bias correction approach, also referred to as ‘histogram equalization’ and/or ‘rank
526 matching’ (Hamlet et al. 2002; Wood et al. 2004; Piani et al. 2010), is useful to statistically
527 transform rainfall simulated by a model to bias corrected data.

528 In this study, the statistics of 24-hr accumulated rainfall for CCPA and GEFSv12
529 reforecasts were determined independently for each grid point and each lead times over
530 CONUS. For simplicity, the 5-member ensemble means for Day-1, 5, 10, and 15 forecasts
531 during the 2002-2019 period were used for this practice. The method can also be applied to the
532 individual ensemble members. The corresponding sample size at each grid point and each lead
533 time is 6574 days. The rainfall intensity distributions for both CCPA and GEFSv12 reforecasts
534 are well approximated by the gamma distribution. The leave-one-out-cross-validation
535 procedure has been implemented. For example, 2019 forecasts are trained using 2002-2018.

536 The bias-corrected procedure is to do a transformation between CCPA cumulative
537 distribution function (CDF) and reforecast CDF, rather than explicitly to calculate bias. The
538 formula for the calibration for a particular lead time (t) and grid (i, j) is expressed as follows:

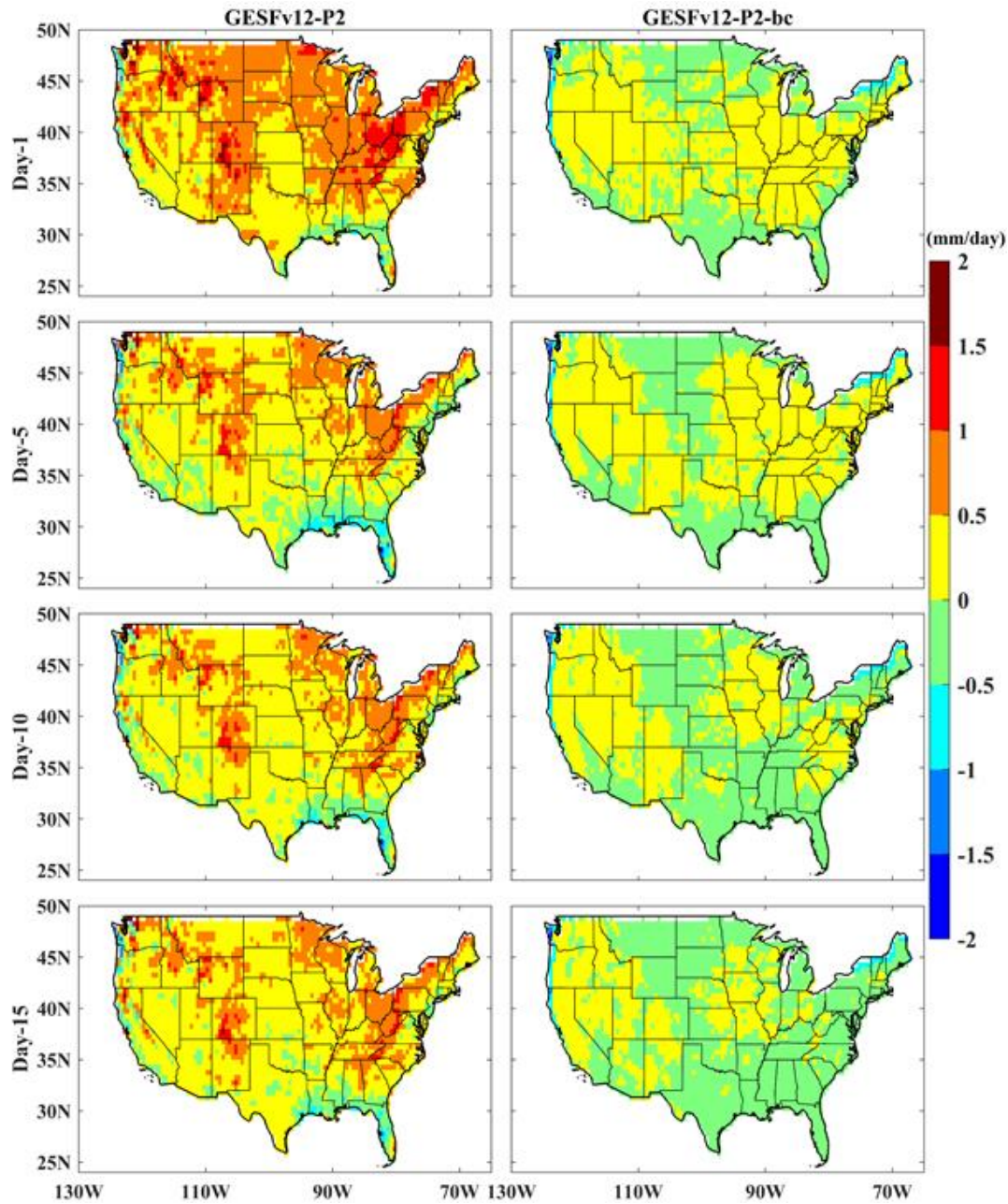
$$539 Q_{bc}(i, j, t) = F_{CCPA}^{-1}(F_{GEFSv12}(Q_{raw}(i, j, t))) \quad (1)$$

540 The bias-corrected value (Q_{bc}) is the inverse of the CCPA CDF (F_{CCPA}^{-1}) at the probability
541 corresponding to the reforecast CDF ($F_{GEFSv12}$) for a given raw forecast (Q_{raw}).

542 *b. Application*

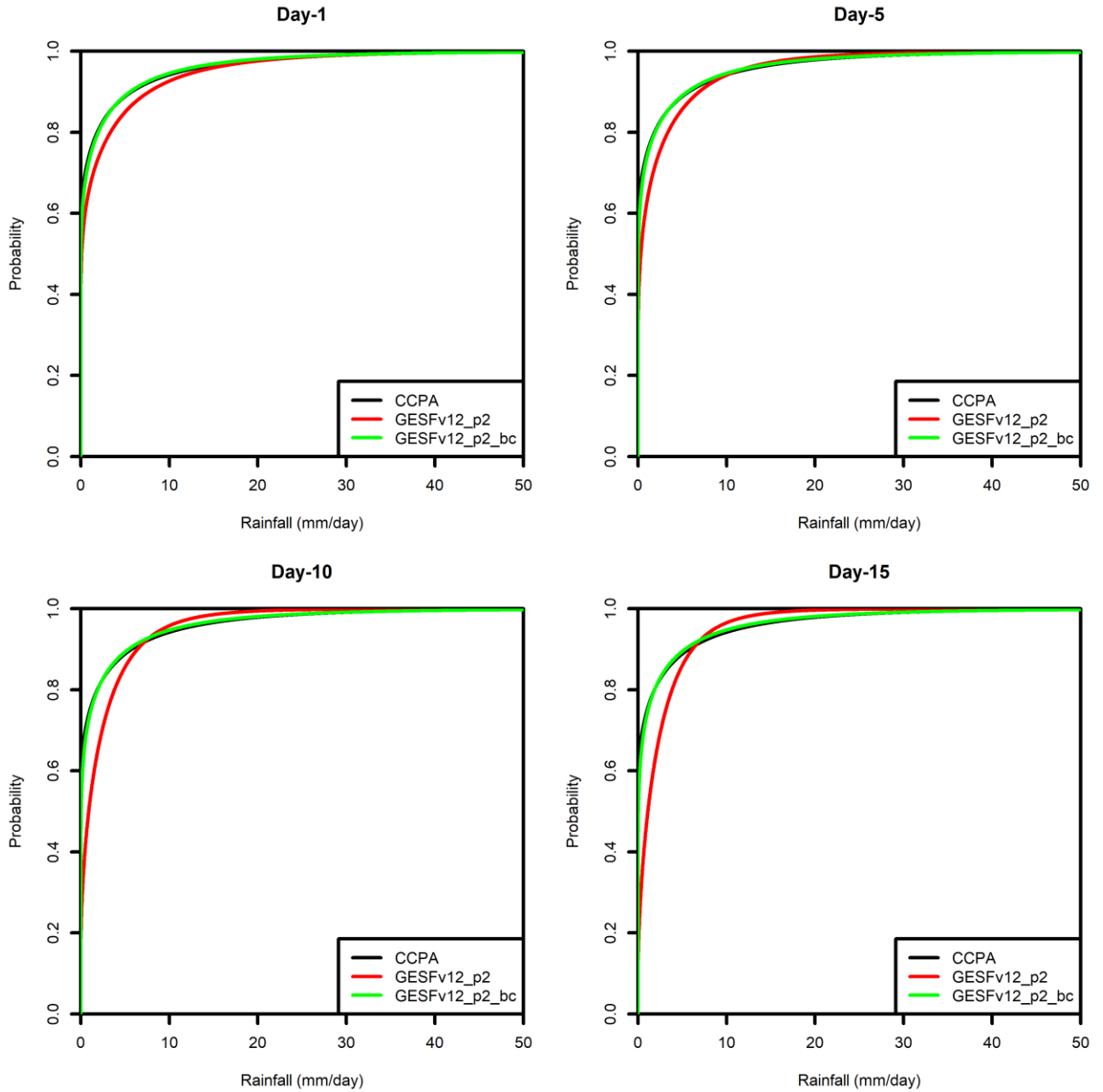
543 Figures 12 and 13 demonstrate that both 24-h precipitation amounts and precipitation
544 probability distributions in the calibrated forecast are more consistent with the CCPA than the
545 raw forecasts. The bias correction dramatically reduces the wet bias over the entire CONUS
546 (Fig. 12). For longer lead times (day 10 and day 15; Fig. 13), the raw forecast tends to
547 underestimate the probability of precipitation less than ~7.5 mm/day and overestimate the
548 corresponding value more than ~7.5 mm/day. After the calibration, the model curves overlap
549 the observed curves for all lead times (Fig. 13). The calibration using long-term reforecast data
550 is particularly important in improving the model climatology for the heavy precipitation events
551 (> 50 mm) as illustrated in Figure 14. In the raw forecast, the model 24-h precipitation events

552 exceeding 50 mm are substantially lower than the CCPA, especially for the longer lead times,
553 when heavy (or extreme) precipitation events are completely missed for most of the domain.
554 After the bias correction, both distributions and magnitudes in heavy precipitation events are
555 much more consistent with the CCPA throughout all lead times.



556
557

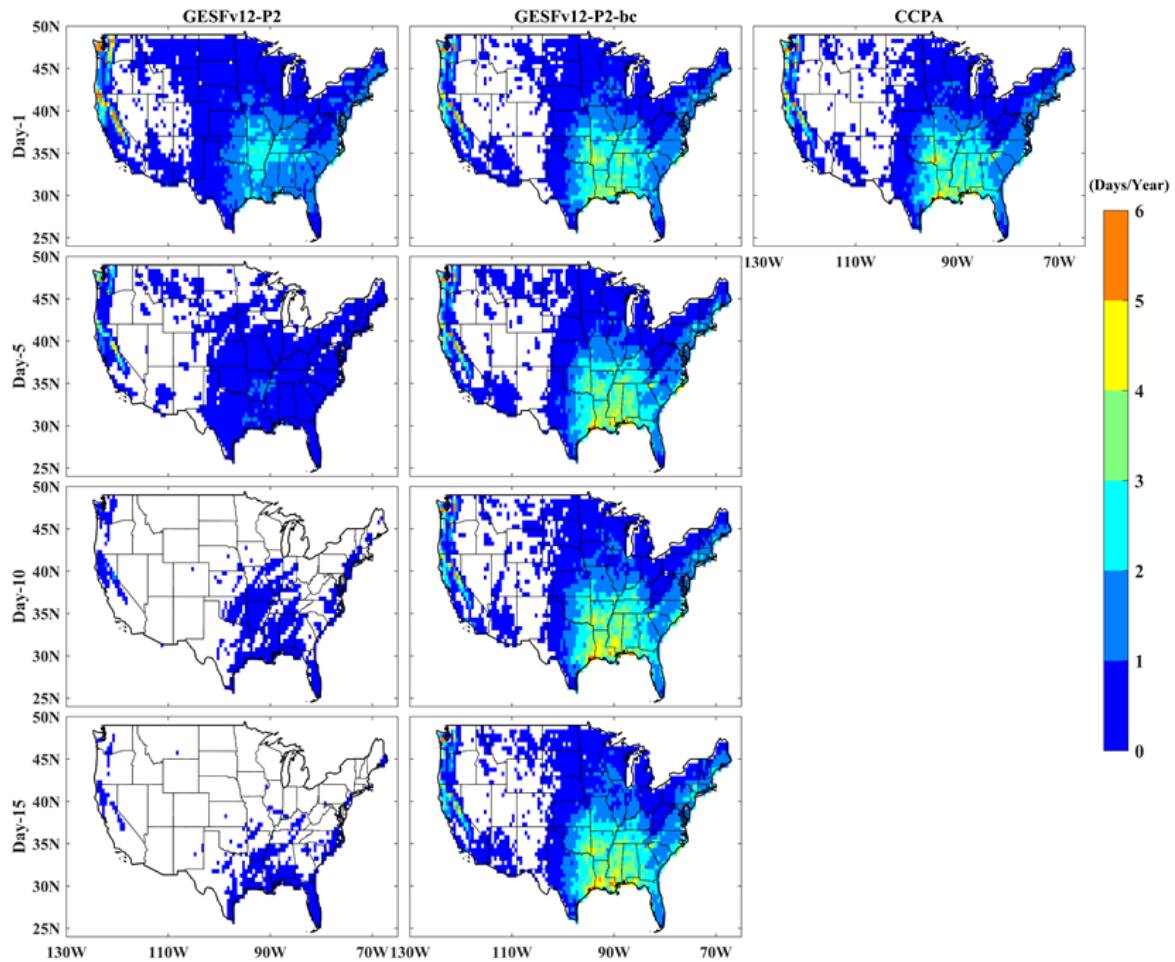
558 Figure 12. The Day-1, Day-5, Day-10, and Day-15 (Row-1 to 4, respectively) biases for
559 24-h precipitation from the (5 member) raw (GEFSv12_p2, left panels) and calibrated
560 (GEFSv12_p2-bc, right panels) ensemble mean forecasts over the CONUS.
561



562
563

564 Figure 13. The Day-1, Day-5, Day-10, and Day-15 probability distributions of 24-h
565 accumulated precipitation for CCPA (black lines), raw (red lines), and bias-corrected (green
566 lines) 5-member ensemble mean forecasts over the full CONUS domain.

567
568
569



570
571

572 Figure 14. The days/year with 24-h precipitation exceeding 50 mm over the CONUS for raw
573 (GEFSv12_p2, Column 1), bias-corrected (GEFSv12_p2-bc, Column 2) 5-member ensemble
574 mean forecasts for Day-1, Day-5, Day-10 and Day-15 and CCPA (Column 3).

575

576 6. Summary

577

578 For the first time, the simultaneous generation of a multi-decade reanalysis and
579 reforecast dataset became part of an operational GEFS implementation. The reforecast dataset
580 is particularly important, considering the extension to subseasonal forecast time scale in the
current GEFSv12. Statistical postprocessing with a long-term training sample of the reforecast

581 has become a routine part of making subseasonal operational outlooks due to the larger forecast
582 errors that exist at longer lead times. The dataset is being used to support several stakeholders
583 in developing their operational products across many time scales. This large volume dataset is
584 easily accessible by both the stakeholders and public users from the NCEP local machines and
585 two public websites. Doubtlessly, this will further facilitate analysis and contributions to model
586 developments.

587 The performance of several selected weather elements, hurricane track, and MJO in the
588 GEFSv12 reforecast were compared with the GEFS_SubX and GEFSv10 reforecasts. The
589 error characterization of the 2-m temperature forecast was analyzed. Overall, the forecast skill
590 for the GEFSv12 is similar to or better than the GEFS_SubX in 500-hpa geopotential height,
591 precipitation, and MJO forecasts. It is also worth mentioning that the degree of some of these
592 improvements is less than those resulting from the change from the GEFSv11 to GEFS_SubX.
593 It should be emphasized that when the GEFS_SubX was developed, considerable efforts were
594 made to enhance the stochastic physics, surface boundary conditions and convection. These
595 model enhancements resulted in substantial improvements in model performance compared to
596 the GEFSv11 (Zhu et al. 2018; Li et al. 2019, Guan et al. 2019). Therefore, when using
597 GEFS_SubX as a benchmark to evaluate GEFSv12_p2, it should be noted that the
598 GEFS_SubX is a difficult model to outperform substantially. The two sets of nearly three
599 decades of reforecast data (GEFSv10 and GEFSv12) provide a good opportunity to address
600 the impacts of the model and analysis on hurricane track forecasts. The initial analysis plays
601 an important role in the accuracy of the track forecast for lead times shorter than about 5 days.
602 The improvement in the model itself may be a potential direction to take in reducing the track
603 forecast error for lead times longer than 5 days, which is a persistent challenge for the NCEP
604 GEFS.

605 In comparison with the GEFS_SubX, the GEFSv12 substantially reduces the warm (cold)
606 bias over the NA domain during the boreal warm (cold) season. However, the cold bias for the
607 cold season in the GEFSv12 is still considerable. Further analysis of the error characteristics
608 demonstrates that this bias is snow-dependent, emphasizing the importance of 2-m temperature
609 calibration for GEFSv12 based on the existence of snow cover. The multi-decadal reforecast

610 dataset was also demonstrated to be very useful in calibrating the precipitation and capturing
611 extreme precipitation events.

612

613 **Acknowledgements**

614 We thank Dr. Hui-Ya Zhuang and Wesley Ebisuzaki and Leigh Zhang for providing
615 valuable helps on the NCEP post package and wgrib2 utility. We also acknowledge Dr. Yan
616 Luo for supplying the CCPA data. We are grateful to Dr. Mark Fresch, James Ward, and
617 Yuqiong Liu in the National Water Center for their careful reviews of the reforecast's
618 precipitation dataset. Special appreciation goes to Mary Hart for editing the English and Lydia
619 Stefanova and Weizhong Zheng for giving the good comments and suggestions through the
620 internal review process in EMC. This study is partially supported through NOAA Weather
621 Program Office grant T8R1CRS-PCR, NOAA Climate Program Office grants S8R1CWS-PRE
622 and R8R1CWS-P01, NWS OSTI grants P8MWQNG-PTR, P8R1MP1-PPS, and M8M6H81-
623 P10, and OAR/WPO-NWS-EMC-SLA. Jonathan Brannock of the North Carolina Institute for
624 Climate Studies assisted with the transfer of reforecast data to Amazon Web Services under
625 NOAA Big Data Program.

626 **Data availability statement**

627 The GEFSv12 Phase-2 reforecast data are openly available at NOAA/NWS/NCEP's
628 ftp server (<ftp://ftp.emc.ncep.noaa.gov/GEFSv12/reforecast>) and Amazon Web Services
629 (AWS, <https://noaa-gefs-retrospective.s3.amazonaws.com/index.html>). The 22 variables for
630 the Phase 1 reforecast are also openly available at NOAA/NWS/NCEP's ftp server
631 (<ftp://ftp.emc.ncep.noaa.gov/GEFSv12/reforecast>).

632

633 **REFERENCES**

634 Alpert, J., M. Kanamitsu, P. M. Caplan, J. G. Sela, G. H. White, and E. Kalnay, 1988: Mountain
635 induced gravity wave drag parameterization in the nmc medium-range forecast model. p726–
636 733, Baltimore, MD, Eighth Conf. on Numerical Weather Prediction, Amer. Meteor. Soc.

637

638 Baxter, M. A., G. M. Lackmann, K. M. Mahoney, T. E. Workoff, and T. M. Hamill, 2014:
639 [Verification of precipitation reforecasts over the Southeast United States.](#) *Wea. Forecasting*,
640 **29**, 1199-1207.

641

642 Berner, J., and others, 2017: Stochastic Parameterization: Toward a New View of Weather and
643 Climate Models, *Bulletin of the American Meteorological Society*, 98(3), 565-588. Retrieved
644 Aug 31, 2021, from [https://journals.ametsoc.org/view/journals/bams/98/3/bams-d-15-
645 00268.1.xml](https://journals.ametsoc.org/view/journals/bams/98/3/bams-d-15-00268.1.xml)

646

647 Bloom, S. C., L. L. Takacs, A. M. Da Silva, and D. Ledvina, 1996: Data assimilation using
648 incremental analysis updates. *Mon. Wea. Rev.*, **124**, 1256–1271, doi:10.1175/1520-
649 0493(1996)124<1256:DAUIAU>2.0.CO;2.

650

651 Brier, G. W., 1950: Verification of forecasts expressed in terms of probability. *Mon. Wea. Rev.*,
652 **78**, 1–3.

653

654 Buizza, R., M. Miller, and T. Palmer, 1999: Stochastic representation of model uncertainties
655 in the ECMWF Ensemble Prediction System. *Quart. J. Roy. Meteor. Soc.*, 125, 2887–
656 2908, <https://doi.org/10.1002/qj.49712556006>.

657

658 Candille, G., 2009: The multiensemble approach: The NAEFS example. *Mon. Wea. Rev.*, 137,
659 1655–1665, <https://doi.org/10.1175/2008MWR2682.1>.

660

661 —, S. Beauregard, and N. Gagnon, 2010: Bias correction and multiensemble in the NAEFS
662 context or how to get a “free calibration” through a multiensemble approach. *Mon. Wea. Rev.*,
663 138, 4268–4281, <https://doi.org/10.1175/2010MWR3349.1>.

664

665 Chen, F., K. Mitchell, J. Schaake, Y. Xue, H.-L. Pan, V. Koren, Q.-Y. Duan, M. Ek, and A.
666 Betts, 1996: Modeling of land-surface evaporation by four schemes and comparison with FIFE
667 observations, *J. Geophys. Res.*, 101(D3), 7251–7268, doi:10.1029/95JD02165.
668

669 Chun, H. Y., and J. J. Baik, 1998: Momentum flux by thermally induced internal gravity waves
670 and its approximation for large-scale models, *J. Atmos. Sci.*, 55, 3299–3310.
671

672 Clough, S. A., M. W. Shephard, E. J. Mlawer, J. S. Delamere, M. J. Iacono, K. Cady-Pereira,
673 S. Boukabara, and P. D. Brown, 2005: Atmospheric radiative transfer modeling: A summary
674 of the AER codes, *J. Quant. Spectrosc. Radiat. Transfer*, 91, 233–244,
675 doi:10.1016/j.jqsrt.2004.05.058.
676

677 Demargne, J., Wu, L., Regonda, S. K., Brown, J. D., Lee, H., He, M., Seo, D., Hartman, R.,
678 Herr, H. D., Fresch, M., Schaake, J., & Zhu, Y., 2014: The Science of NOAA's Operational
679 Hydrologic Ensemble Forecast Service, *Bulletin of the American Meteorological Society*,
680 95(1), 79-98. Retrieved Aug 31, 2021, from
681 <https://journals.ametsoc.org/view/journals/bams/95/1/bams-d-12-00081.1.xml>
682

683 Dorman, J. L., and P. J. Sellers, 1989: A global climatology of albedo, roughness length and
684 stomatal resistance for atmospheric general circulation models as represented by the Simple
685 Biosphere model (SiB), *J. Appl. Meteorol.*, 28, 833–855, doi:10.1175/1520-
686 0450(1989)028<0833:AGCOAR>2.0.CO;2.
687

688 Ek, M. B., K. E. Mitchell, Y. Lin, E. Rogers, P. Grunmann, V. Koren, G. Gayno, and J. D.
689 Tarpley, 2003: Implementation of Noah land-surface model advances in the NCEP operational
690 mesoscale Eta model. *J. Geophys. Res.*, 108, 8851, doi:10.1029/2002JD003296.
691

692 Ek, M. B., Y. Xia, J. Meng, R. Shresha, H. Wei, J. Dong, Y. Wu, and W. Zheng, 2016; Land
693 Prediction in NCEP Modeling Systems: Current Status and Future Plans,
694 weather.gov/media/sti/nggps/10_Ek%20EMC-land-NGGPS-Feb2016.pdf.
695
696 EMCs, 2019: GFS v15 implementation in June 2019. Ref:
697 https://www.emc.ncep.noaa.gov/emc/pages/numerical_forecast_systems/gfs.php.
698
699 Emerton, R., E. Zsoter, L. Arnal, H. L. Cloke, D. Muraro, C. Prudhomme, E.M. Stephens, P.
700 Salamon, and F. Pappenberger, 2018: Developing a global operational seasonal hydro-
701 meteorological forecasting system: GloFAS-Seasonal v1.0. *Geosci. Model Dev.*, **11**, 3327–
702 3346. DOI: <https://doi.org/10.5194/gmd-11-3327-2018>.
703
704 Galarnau, T. J., Jr., and Hamill, T. M., 2015: Diagnosis of track forecast errors for tropical
705 cyclone Rita, 2005: Using GEFS reforecasts, *Weather and Forecasting*, **30**(5), 1334-1354.
706 Retrieved Aug 31, 2021, from [https://journals.ametsoc.org/view/journals/wefo/30/5/waf-d-15-](https://journals.ametsoc.org/view/journals/wefo/30/5/waf-d-15-0036_1.xml)
707 [0036_1.xml](https://journals.ametsoc.org/view/journals/wefo/30/5/waf-d-15-0036_1.xml)
708
709 Gascon, E., D. Lavers, D., T. M. Hamill, D. S. Richardson, Z. Ben Bouallegue, M. Leutbecher,
710 and F. Pappenberger, 2019: [Statistical post-processing of dual-resolution ensemble](#)
711 [precipitation forecasts across Europe](#). *Quart. J. Royal Meteor. Soc.*, 1-18,
712 <https://doi.org/10.1002/qj.3615>.
713
714 Guan, H., B. Cui, and Y. Zhu, 2015: Improvement of statistical postprocessing using GEFS
715 reforecast information. *Wea. Forecasting*, **30**, 841–854, [https://doi.org/10.1175/WAF-D-14-](https://doi.org/10.1175/WAF-D-14-00126.1)
716 [00126.1](https://doi.org/10.1175/WAF-D-14-00126.1).
717
718 Guan, H., and Y. Zhu, 2017: Development of verification methodology for extreme weather
719 forecasts. *Wea. Forecasting*, **32**, 479–491, <https://doi.org/10.1175/WAF-D-16-0123.1>.
720

721 Guan, H., Y. Zhu, E. Sinsky, W. Li, X. Zhou, D. Hou, C. Melhauser, and R. Wobus, 2019:
722 Systematic Error Analysis and Calibration of 2-m Temperature for the NCEP GEFS Reforecast
723 of the Subseasonal Experiment (SubX) Project. *Wea. Forecasting*, 34, 361–376,
724 <https://doi.org/10.1175/WAF-D-18-0100.1>.
725

726 Hagedorn, R., 2008: Using the ECMWF reforecast dataset to calibrate EPS forecasts. ECMWF
727 Newsletter 117, 8-13.
728

729 Hagedorn, R., R. Buizza, T. M. Hamill, M. Leutbecher, and T. N. Palmer, 2012: [Comparing](#)
730 [TIGGE multi-model forecasts with reforecast-calibrated ECMWF ensemble forecasts.](#) *Quart*
731 *J. Royal Meteor Soc.*, **138**, 1814-1827.
732

733 Hagedorn, R., T. M. Hamill, and J. S. Whitaker, 2008: Probabilistic forecast calibration using
734 ECMWF and GFS ensemble reforecasts. Part I: 2-meter temperature. *Mon. Wea. Rev.*, **136**,
735 2608-2619.
736

737 Hamill, T. M., and J. S. Whitaker, 2006: Probabilistic quantitative precipitation forecasts based
738 on reforecast analogs: Theory and application. *Mon. Wea. Rev.*, **134**, 3209–3229.
739

740 Hamill, T. M., J. S. Whitaker, and S. L. Mullen, 2006: Reforecasts, an important dataset for
741 improving weather predictions. *Bull. Amer. Meteor. Soc.*, **87**, 33-46.
742

743 Hamill, T. M., J. S. Whitaker, and X. Wei, 2004: Ensemble reforecasting: Improving medium-
744 range forecast skill using retrospective forecasts. *Mon. Wea. Rev.*, **132**, 1434–1447,
745 [https://doi.org/10.1175/1520-0493\(2004\)132<1434:ERIMFS>2.0.CO;2](https://doi.org/10.1175/1520-0493(2004)132<1434:ERIMFS>2.0.CO;2).
746

747 Hamill, T. M., R. Hagedorn, and J. S. Whitaker, 2008: Probabilistic forecast calibration using
748 ECMWF and GFS ensemble reforecasts. Part II: Precipitation. *Mon. Wea. Rev.*, **136**, 2620–
749 2632.

750

751 Hamill, T. M., 2012: Verification of TIGGE Multi-model and ECMWF reforecast-calibrated
752 probabilistic precipitation forecasts over the conterminous US. *Mon. Wea. Rev.*, **140**, 2232-
753 2252.

754

755 Hamill T. M., G. T. Bates, J. S. Whitaker, D. R. Murray, M. Fiorino, T. J. Galarneau, Jr., Y.
756 Zhu, and W. Lapenta, 2013: NOAA's Second-Generation Global Medium-Range Ensemble
757 Reforecast Data Set. *Bull. Amer. Meteor. Soc.*, **94**(10), 1553-1565.

758

759 Hamill, T. M., and G. N. Kiladis, 2013: Skill of the MJO and Northern Hemispheric blocking
760 in GEFS medium-range reforecasts. *Mon. Wea. Rev.*, **142**, 686-885.

761

762 Hamill, T. M., M. Scheuerer, and G. T. Bates, 2015: Analog probabilistic precipitation
763 forecasts using GEFS Reforecasts and Climatology-Calibrated Precipitation Analyses. *Mon.*
764 *Wea. Rev.*, **143**, 3300-3309.

765

766 Hamill, T. M., 2017: Changes in the systematic errors of global reforecasts due to an evolving
767 data assimilation system. *Mon. Wea. Rev.*, **145**, 2479-2485.

768

769 Hamill, T. M., and Scheuerer, M., 2018: Probabilistic precipitation forecast postprocessing
770 using quantile mapping and rank-weighted best-member dressing. *Mon. Wea. Rev.*, **146**, 4079-
771 4098.

772

773 Hamill, T. M., and Coauthors, 2021: The Reanalysis for the Global Ensemble Forecast
774 System, version 12. *Mon. Wea. Rev.*, conditionally accepted.

775

776 Hamlet, A. F., Huppert, D., and Lettenmaier, D. P., 2002: The economic value of long-lead
777 streamflow forecasts for Columbia River hydropower. *Journal of Water Resources Planning*

778 and Management, 128(2):91–101, [https://doi.org/10.1061/\(ASCE\)0733-9496\(2002\)128:2\(91\)](https://doi.org/10.1061/(ASCE)0733-9496(2002)128:2(91)).
779
780
781 Han, J., and Pan, H.-L., 2011: Revision of convection and vertical diffusion schemes in the
782 NCEP Global Forecast System. *Wea. Forecasting*, 26(4), 520– 533.
783
784 Han, J., W. Wang, Y. C. Kwon, S.-Y. Hong, V. Tallapragada, and F. Yang, 2017: Updates in
785 the NCEP GFS cumulus convection schemes with scale and aerosol awareness. *Wea.*
786 *Forecasting*, 32, 2005–2017, <https://doi.org/10.1175/WAF-D-17-0046.1>.
787
788 Han, J., M. Witek, J. Teixeira, R. Sun, H.-L. Pan, J. K. Fletcher, and C. S. Bretherton,
789 2016: Implementation in the NCEP GFS of a Hybrid Eddy-Diffusivity Mass-Flux (EDMF)
790 boundary layer parameterization with dissipative heating and modified stable boundary layer
791 mixing. *Wea. Forecasting*, **31**, 341–352, <https://doi.org/10.1175/WAF-D-15-0053.1>.
792
793 Harris, L. M., & Lin, S. J. 2013: A two-way nested global-regional dynamical core on the
794 cubed-sphere grid. *Mon. Wea. Rev.*, 141(1), 283– 306.
795
796 Hou, D., M. Charles, Y. Luo, Z. Toth, Y. Zhu, R. Krzysztofowicz, Y. Lin, P. Xie, D-J. Seo,
797 M. Pena and B. Cui, 2014: Climatology-Calibrated Precipitation Analysis at Fine Scales:
798 Statistical Adjustment of Stage IV toward CPC Gauge-Based Analysis. *J. Hydrometeorology*,
799 15, 2542–2557.
800
801 Ines AVM and Hansen J W., 2006: Bias correction of daily GCM rainfall for crop simulation
802 studies. *Agricultural and Forest Meteorology* 138: 44– 53.
803
804 Koren, V., J. Schaake, K. Mitchell, Q.-Y. Duan, F. Chen, and J. Baker, 1999: A
805 parameterization of snowpack and frozen ground intended for NCEP weather and climate
806 models, *J. Geophys. Res.*, 104(D16), 19,569– 19,585, doi:10.1029/1999JD900232.

807

808 Lalaurette, F., 2003: Early detection of abnormal weather conditions using a probabilistic
809 extreme forecast index. *Quart. J. Royal Meteorol. Soc.*, **129**, 3037-3057.
810 <https://doi.org/10.1256/qj.02.152>

811

812 Landsea, C. W., and J. P. Cangialosi, 2018: Have we reached the limits of predictability for
813 tropical cyclone track forecasting? *Bull. Meteor. Amer. Soc.*, **99**, 2237–2243,
814 <https://doi.org/10.1175/BAMS-D-17-0136.1>.

815

816 Li, W., Y. Zhu, X. Zhou, D. Hou, E. Sinsky, C. Melhauser, M. Pena, H. Guan and R. Wobus,
817 2019: Evaluating the MJO forecast skill from different configurations of NCEP GEFS
818 extended forecast. *Clim. Dyn.*, <https://doi.org/10.1007/s00382-018-4423-9>.

819

820 Lin, S.-J., 2004: A “vertically Lagrangian” finite-volume dynamical core for global models.
821 *Mon. Wea. Rev.*, **132**, 2293–2307.

822

823 Lin, S.-J., and R. B. Rood, 1997: An explicit flux-form semi-Lagrangian shallow-water model
824 on the sphere, *Q. J. R. Meteor. Soc.*, **123**:2477-2498.

825

826 Long, P. J., 1984: An general unified similarity theory for the calculation of turbulent fluxes
827 in the numerical weather prediction models for unstable condition. Office Note 302, U.S.
828 Department of Commerce, National Oceanic and Atmospheric Administration, National
829 Weather Service, National Meteorological Center, 30 pp.

830

831 ———, 1986: An economical and compatible scheme for parameterizing the stable surface layer
832 in the medium-range forecast model. Office Note 321, U.S. Department of Commerce,
833 National Oceanic and Atmospheric Administration, National Weather Service, National
834 Meteorological Center, 24 pp.

835

836 Luo Y., Y. Zhu, D. Hou, Y. Lin, P. Xie, 2018: The NCEP's Climatology-Calibrated
837 Precipitation Analysis (CCPA) Version 4. *In the 98th American Meteorological Society*
838 *Annual Meeting, AMS.*
839

840 Mitchell, K. E., H. Wei, S. Lu, G. Gayno, and J. Meng, 2005: NCEP implements major upgrade
841 to its medium-range global forecast system, including land-surface component, *GEWEX News*
842 15(4), 8–9. [Available at <http://www.gewex.org/Nov2005.pdf>.]
843

844 Nardi, K. M., E. A. Barnes and F. M. Ralph, 2018: Assessment of numerical weather prediction
845 model reforecasts of the occurrence, intensity, and location of atmospheric Rivers along the
846 west coast of North America. *Mon. Wea. Rev.*, 146, 3343– 3362.
847 <https://doi.org/10.1175/MWR-D-18-0060.1>.
848

849 Noh, Y.-C.; Lim, A.H.N.; Huang, H.-L.; Goldberg, M. D., 2020: Global Forecast Impact of
850 Low Data Latency Infrared and Microwave Sounders Observations from Polar Orbiting
851 Satellites. *Remote Sens.* **2020**, 12, 2193. <https://doi.org/10.3390/rs12142193>
852

853 Ou, M., M. Charles, and D. Collins, 2016: Sensitivity of calibrated week-2 probabilistic
854 forecast skill to reforecast sampling of the NCEP Global Ensemble Forecast System. *Wea.*
855 *Forecasting*, **31**, 1093–1107, <https://doi.org/10.1175/WAF-D-15-0166.1>.
856

857 Palmer, T. N., 2001: A nonlinear dynamical perspective on model error: A proposal for non-
858 local stochastic-dynamic parameterization in weather and climate prediction. *Quart. J. Roy.*
859 *Meteor. Soc.*, **127**, 279–304, doi:10.1002/qj.49712757202
860

861 Palmer, T. N. Buizza, F. Doblas Reyes, T. Jung, M. Leutbecher, G. Shutts, M. Steinheimer,
862 and A. Weisheimer, 2009: Stochastic parametrization and model uncertainty. *ECMWF Tech.*
863 *Memo.* 598, 42 pp., <http://www.ecmwf.int/publications/>.
864

865 Palmer, T. N., 2012: Towards the probabilistic Earth-system simulator: A vision for the future
866 of climate and weather prediction. *Quart. J. Roy. Meteor. Soc.*, **138**, 841–861, doi:10.1002/q
867 j.1923.

868

869 Pegion, K., and Coauthors, 2019: The Subseasonal Experiment (SubX): A multi-model
870 subseasonal prediction experiment. *Bull. Amer. Meteor. Soc.*, 100, 2043–2060.
871 <https://doi.org/10.1175/BAMS-D-18-0270.1>

872

873 Piani, C., J. Haerter, and E. Coppola, 2010: Statistical bias correction for daily precipitation
874 in regional climate models over Europe. *Theor. Appl. Climatol.*, 99(1-2), 187-192,
875 <https://doi.org/10.1007/s00704-009-0134-9>

876

877 Putman, W. M., S.-J. Lin, 2007: Finite-volume transport on various cubed-sphere grids. *J.*
878 *Computational Phys.*, 227, 55-78, <https://doi.org/10.1016/j.jcp.2007.07.022>.

879

880 Reynolds, R. W., N. A. Rayner, T. M. Smith, D.C. Stokes, and W. Wang, 2002: An
881 improved in situ and satellite SST analysis for climate. *J. Climate*, **15**, 1609-1625.

882

883 Saha, S., and Coauthors, 2010: The NCEP Climate Forecast System Reanalysis. *Bull. Amer.*
884 *Meteor. Soc.*, 91, 1015-1057. doi: 10.1175/2010BAMS3001.1.

885

886 Schmeits, M. J., K. J. Kok, 2010: A Comparison between Raw Ensemble Output, (Modified)
887 Bayesian Model Averaging, and Extended Logistic Regression Using ECMWF Ensemble
888 Precipitation Reforecasts, *Mon. Wea. Rev.*, vol. 138, 4199–4211.

889

890 Scheuerer, M., and T. M. Hamill, 2015: Statistical post-processing of ensemble precipitation
891 forecasts by fitting censored, shifted Gamma distributions. *Mon. Wea. Rev.*, **143**, 4578-4596.
892 Also appendix A and appendix B and appendix C.

893 Scheuerer, M., and Hamill, T.M., 2018: Generating calibrated ensembles of physically
894 realistic, high-resolution precipitation forecast fields based on GEFS model output. *J.*
895 *Hydrometeorology*, **19** (10), 1651-1670. <https://journals.ametsoc.org/doi/abs/10.1175/JHM->
896 [D-18-0067.1](https://journals.ametsoc.org/doi/abs/10.1175/JHM-D-18-0067.1)
897

898 Scheuerer, M., M. B. Switanek, R. P. Worsnop, and T. M. Hamill, 2020: Using Artificial
899 Neural Networks for Generating Probabilistic Subseasonal Precipitation Forecasts over
900 California. *Mon. Wea. Rev.*, **148**, 3489-3506, <https://doi.org/10.1175/MWR-D-20-0096.1>.
901

902 Shutts, G., 2005: A kinetic energy backscatter algorithm for use in ensemble prediction
903 systems. *Q.J. Roy. Meteor. Soc.*, 131, 3079–3102, <https://doi.org/10.1256/qj.04.106>.
904

905 Shutts, G. and T. N. Palmer, 2004: The use of high-resolution numerical simulations of
906 tropical circulation to calibrate stochastic physics schemes. Proc. Workshop on Simulation and
907 Prediction of Intra-Seasonal Variability with Emphasis on the MJO, Reading, United
908 Kingdom, ECMWF, 83-102, [https://www.ecmwf.int/en/learning/workshops-and-](https://www.ecmwf.int/en/learning/workshops-and-seminars/past-workshops/2003-simulation-prediction-intra-seasonal-variability)
909 [seminars/past-workshops/2003-simulation-prediction-intra-seasonal-variability](https://www.ecmwf.int/en/learning/workshops-and-seminars/past-workshops/2003-simulation-prediction-intra-seasonal-variability).
910

911 Specq, D., L. Batté, 2020: Improving subseasonal precipitation forecasts through a statistical–
912 dynamical approach: application to the southwest tropical Pacific. *Clim. Dyn.* 55, 1913–1927.
913 <https://doi.org/10.1007/s00382-020-05355-7>.
914

915 Wei, M., Z. Toth, R. Wobus, and Y. Zhu, 2008: Initial perturbations based on the ensemble
916 transform (ET) technique in the NCEP global operational forecast system. *Tellus*, 60A, 62–
917 79, <https://doi.org/10.1111/j.1600-0870.2007.00273.x>.
918

919 Wheeler, M. C., and H. Hendon, 2004: An all-season real-time multivariate MJO index:
920 Development of an index for monitoring and prediction. *Mon. Wea. Rev.*, **132**, 1917–1932,
921 [https://doi.org/10.1175/1520-0493\(2004\)132<1917:AARMMI>2.0.CO;2](https://doi.org/10.1175/1520-0493(2004)132<1917:AARMMI>2.0.CO;2).

922

923 Wilks, D. S., 1995: Statistical Methods in the Atmospheric Sciences. Academic Press.

924

925 Wilks, D. S., and T. M. Hamill, 2007: [Comparison of ensemble-MOS methods using GFS](#)
926 [reforecasts](#). *Mon. Wea. Rev.*, **135**, 2379-2390.

927

928 Wood, A. W., L. R. Leung, V. Sridhar, and D. Lettenmaier, 2004: Hydrologic implications of
929 dynamical and statistical approaches to downscaling climate model outputs. *Climatic change*,
930 62(1-3), 189-216, <https://doi.org/10.1023/B:CLIM.0000013685.99609.9e>.

931

932 Zheng, W., H. Wei, Z. Wang, X. Zeng, J. Meng, M. Ek, K. Mitchell, and J. Derber, 2012:
933 Improvement of daytime land surface skin temperature over arid regions in the NCEPGFS
934 model and its impact on satellite data assimilation. *J. Geophys. Res.*, 117, D06117,
935 doi:10.1029/2011JD015901.

936

937 Zheng, W., Ek, M., Mitchell, K., Wei, H., and Meng, J., 2017: Improving the stable surface
938 layer in the NCEP global forecast system. *Monthly Weather Review*, 145, 3969– 3987.
939 <https://doi.org/10.1175/mwr-d-16-0438.1>.

940

941 Zhou, X., Y. Zhu, B. Fu, D. Hou, J. Peng, Y. Luo and W. Li, 2019: The development of Next
942 NCEP Global Ensemble Forecast System. *STI Climate Bulletin*, 159-163.

943

944 Zhou, X., Y. Zhu, D. Hou, B. Fu, W. Li, H. Guan, E. Sinsky, W. Kolczynski, X. Xue, Y. Luo,
945 J. Peng, B. Yang, V. Tallapragada and P. Pegion, 2021: The introduction of the NCEP Global
946 Ensemble Forecast System Version 12. Submitted to *Wea. Forecasting*.

947

948 Zhu, Y, D. Hou, M. Wei, R. Wobus, J. Ma, B. Cui, and S. Moorthi, 2012: GEFS upgrade (v10)
949 at NWS/NCEP/Environmental Modeling Center. [Available online at
950 http://www.emc.ncep.noaa.gov/gmb/yzhu/html/imp/201109_imp.html.]

951

952 Zhu, Y., X. Zhou, M. Pena, W. Li, C. Melhauser, and D. Hou, 2017: Impact of sea surface
953 temperature forcing on weeks 3 and 4 forecast skill in the NCEP Global Ensemble Forecast
954 System. *Wea. Forecasting*, 32, 2159–2173, <https://doi.org/10.1175/WAF-D-17-0093.1>.

955

956 Zhu, Y., and Coauthors, 2018: Toward the improvement of sub-seasonal prediction in the
957 NCEP Global Ensemble Forecast System (GEFS). *J. Geophys. Res.: Atmos.*, **123**, 6732–6745,
958 <https://doi.org/10.1029/2018JD028506>.

959

960 Zobler, L., 1986: A world soil file for global climate modelling, *NASA Tech. Memo.*, TM-
961 87802, 33 pp.

962 Zobler, L., 1999: Global soil types, 1-degree grid (Zobler), <http://www.daac.ornl.gov>,
963 Distrib. Active Arch. Cent. for Biogeochem. Dyn., Oak Ridge Natl. Lab., Oak Ridge, Tenn.,
964 doi:10.3334/ORNLDAAC/418.